SANDIA REPORT

SAND2005-1408
Unlimited Release
Printed March 2005

Final Report on LDRD Project: Outstanding Challenges for AlGaInN MOCVD

J. R. Creighton, D. D. Koleske, G. T. Wang, M. E. Coltrin, A. A. Allerman, M. J. Russell, K. C. Cross, C. C. Mitchell, S. R. Lee, and D. M. Follstaedt

Prepared by
Sandia National Laboratories
Albuquerque, New Mexico 87185 and Livermore, California 94550

Sandia is a multiprogram laboratory operated by Sandia Corporation,
a Lockheed Martin Company, for the United States Department of Energy's
National Nuclear Security Administration under Contract DE-AC04-94AL85000.

Approved for public release; further dissemination unlimited.

Issued by Sandia National Laboratories, operated for the United States Department of Energy by Sandia Corporation.

NOTICE: This report was prepared as an account of work sponsored by an agency of the United States Government. Neither the United States Government, nor any agency thereof, nor any of their employees, nor any of their contractors, subcontractors, or their employees, make any warranty, express or implied, or assume any legal liability or responsibility for the accuracy, completeness, or usefulness of any information, apparatus, product, or process disclosed, or represent that its use would not infringe privately owned rights. Reference herein to any specific commercial product, process, or service by trade name, trademark, manufacturer, or otherwise, does not necessarily constitute or imply its endorsement, recommendation, or favoring by the United States Government, any agency thereof, or any of their contractors or subcontractors. The views and opinions expressed herein do not necessarily state or reflect those of the United States Government, any agency thereof, or any of their contractors.

Printed in the United States of America. This report has been reproduced directly from the best available copy.

Available to DOE and DOE contractors from
U.S. Department of Energy
Office of Scientific and Technical Information
P.O. Box 62
Oak Ridge, TN 37831

Telephone: (865)576-8401
Facsimile: (865)576-5728
E-Mail: reports@adonis.osti.gov
Online ordering: http://www.osti.gov/bridge

Available to the public from
U.S. Department of Commerce
National Technical Information Service
5285 Port Royal Rd
Springfield, VA 22161

Telephone: (800)553-6847
Facsimile: (703)605-6900
E-Mail: orders@ntis.fedworld.gov
Online order: http://www.ntis.gov/help/ordermethods.asp?loc=7-4-0#online

SAND2005-1408
Unlimited Release
Printed March 2005

Final Report on LDRD Project: Outstanding Challenges for AlGaInN MOCVD

J.R. Creighton, D.D. Koleske, G.T. Wang, M. E. Coltrin, A.A. Allerman, M.J. Russell, K.C. Cross, C.C. Mitchell
Advanced Materials Sciences Department

S. R. Lee
Semiconductor Material & Device Sciences Department

D. M. Follstaedt
Radiation-Solid Interactions Department

Sandia National Laboratories
P.O. Box 5800
Albuquerque, NM 87185-0601

Abstract

The AlGaInN material system is used for virtually all advanced solid state lighting and short wavelength optoelectronic devices. Although metal-organic chemical vapor deposition (MOCVD) has proven to be the workhorse deposition technique, several outstanding scientific and technical challenges remain, which hinder progress and keep RD&A costs high. The three most significant MOCVD challenges are:

(1) Accurate temperature measurement.
(2) Reliable and reproducible p-doping (Mg).
(3) Low dislocation density GaN material.

To address challenge (1) we designed and tested (on reactor mockup) a multiwafer, dual wavelength, emissivity-correcting pyrometer (ECP) for AlGaInN MOCVD. This system simultaneously measures the reflectance (at 405 and 550 nm) and emissivity-corrected temperature for each individual wafer, with the platen signal entirely rejected. To address challenge (2) we measured the $MgCp_2$ + NH_3 adduct condensation phase diagram from 65-115°C, at typical MOCVD concentrations. Results indicate that it requires temperatures of 80-100°C in order to prevent $MgCp_2$ + NH_3 adduct condensation. Modification and testing of our research reactor will not be complete until FY2005. A new commercial Veeco reactor was installed in early FY2004, and after qualification growth experiments were conducted to improve the GaN quality using a delayed recovery technique, which addresses challenge (3). Using a delayed recovery technique, the dislocation densities determined from x-ray diffraction were reduced from 2×10^9 cm^{-2} to 4×10^8 cm^{-2}. We have also developed a model to simulate reflectance waveforms for GaN growth on sapphire.

Contents

1 Accurate Temperature Measurement (J.R. Creighton, C.C. Mitchell, A.A. Allerman) 6

1.1 Introduction 6

1.2 Optics for the Veeco D-125 MOCVD Reactor 6

1.3 Hardware modifications to the Veeco D-125 MOCVD Reactor 8

1.4 The Data Acquisition System 10

1.5 System Performance 14

1.6 Reference 17

2 Reproducible Magnesium Doping (J.R. Creighton, G.T. Wang) 18

2.1 Introduction 18

2.2 Experimental 19

2.3 QCM Results 20

2.4 References 24

3 Understanding and Improving GaN growth on Sapphire (D. D. Koleske, M. E. Coltrin, S. R. Lee, D. M. Follstaedt, A. A. Allerman, M. J. Russell, K. C. Cross, C. C. Mitchell) 25

3.1 Reducing dislocation density of GaN films on sapphire 25

3.2 Nucleation layer decomposition kinetics and nuclei formation 32

3.2.1 Fitting the Group III Nitride Reflectance Waveform 32

3.2.2 NL Decomposition Kinetics and Kinetic Advancement 35

3.3 Modeling optical reflectance for GaN growth on sapphire 38

3.4 References 42

1 Accurate Temperature Measurement (J.R. Creighton, C.C. Mitchell, A.A. Allerman)

1.1 Introduction

Surface temperature measurement during AlGaInN MOCVD is particularly difficult because the epilayers and substrates (typically sapphire) are transparent at the near-IR wavelengths normally used for pyrometry. One solution is to detect radiation near 400 nm (UV-violet range, or UVV) where the GaN epilayers are opaque at the high temperatures encountered during deposition. A method of emissivity-correction should also be applied to improve the utility and accuracy of pyrometry. In fact, emissivity-correction is almost always necessary due to the optical interference effects that occur during heteroepitaxy.

We previously developed and installed a 1st generation UVV emissivity-correcting pyrometer (ECP) on our research MOCVD reactor (CVD1) [1]. The effective wavelength of this system is 405 nm. Overall performance was excellent, with RMS noise levels well below 0.1°C during the 1050°C GaN deposition step. Simultaneous reflectance measurements [2] yield the growth rate, the high-temperature optical constants for GaN, and demonstrate that the epilayer is indeed opaque (once 0.5-1.0 micron of GaN has been deposited). The system was also configured to simultaneously measure reflectance and thermal emission signals at 550 nm. This wavelength is useful for monitoring growth rates (from the reflectance signal) over long time spans. Temperature measurements at this wavelength, however, are not reliable due to the transparency of the substrate and epilayers.

The primary goal of this task in the 2004 LDRD project was to modify and transfer the UVV-ECP technology to one of our commercial Veeco (formerly Emcore) D-125 MOCVD system. This transfer required significant modifications because the D-125 is a 3-wafer system. A method of synchronizing the detection system with the wafer platen was developed so signals only from the desired wafer(s) could be measured, while rejecting signals from the platen. The D-125 also has more limited optical access, in comparison to CVD1, so the front end optics needed a redesign and optimization.

1.2 Optics for the Veeco D-125 MOCVD Reactor

One challenge is to maximize optical throughput in the more restricted geometry of the D-125 reactors. In CVD1 we were able to use a near normal incidence geometry, where the input optics for the reflectance signal are completely separate from the collection optics. In this configuration, no beam-splitter is required, and the stray reflection signal from the top window can typically be entirely rejected. For the D-125 reactors we are forced to adapt a collinear configuration using a beam-splitter, due to the smaller available viewport (see Fig 1.1). In this configuration a sometimes sizeable reflection signal occurs from the reactor window, and this must be accounted for when computing the wafer reflectance. We have chosen a 70T/30R (70% transmittance, 30% reflectance) beam-splitter as a compromise between thermal emission throughput and reflectance signal throughput. The presence this beam-splitter reduces our thermal emission signal by a factor of ~ 0.7 relative to near-normal incidence configuration.

Another significant loss of signal occurs because the relatively small window diameter (16.7 mm) forces us to reduce the collection lens diameter from 23 mm to 15 mm. There is also

an aperture in the cold plate (15 mm diameter) about half way to the wafer we account for. The collection lens is the solid angle defining aperture in this system, so the lens diameter reduction alone would reduce the signal by ~ 2.4 X. We can regain some signal by reducing the focal length from 35 mm to 30 mm, which increases the detection solid angle (and the image size on the wafer). In the current version of the system the fiber is positioned so its image is projected onto the wafer at a distance of 290 ± 10 mm, which gives an image diameter of 13.5-14 mm. There is not much margin for error here so in the future we may be forced to sacrifice some signal (smaller image size, reduced solid angle) in order to make the system more robust.

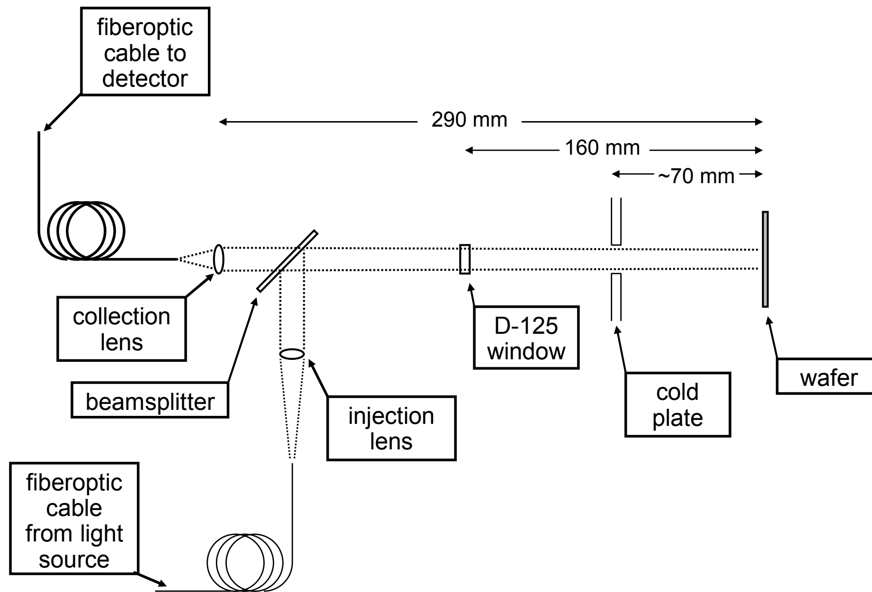

Fig. 1.1. Schematic of D-125 optics.

After taking into account the signal loss due the beam-splitter transmission and reduced solid angle, we expect an overall signal reduction of 2.5-2.9 X. The system was calibrated using a blackbody source and compared to the previous UVV-ECP response curve for our single-wafer system (see Fig. 1.2). The two calibration curves have the same functional form (i.e. effective wavelength), as expected. The D-125 multiwafer system response is 2.6 X smaller than the single wafer system response, in good agreement with our expectations. The magnitude of this signal loss is not of much consequence at high temperatures (~1000°C) where we have abundant signal, but in the 700-800°C range it certainly makes measurements more difficult. Another important signal loss component is the reduced signal duty cycle in a multiwafer system (discussed in the next section).

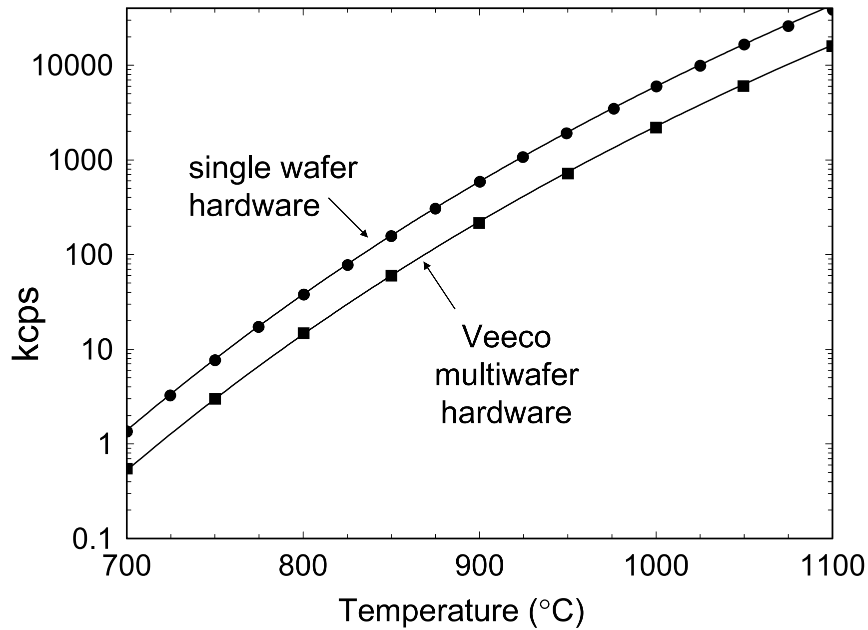

Fig. 1.2. UVV-ECP calibration curves.

1.3 Hardware modifications to the Veeco D-125 MOCVD Reactor

In order to adapt the UVV-ECP to a multiwafer (3 wafers in this case) environment, a method of synchronizing the data acquisition (DAQ) system with the rotation of the wafer platen must be developed. The goal is to collect data (reflectance and temperature) only from the wafers, while rejecting the signal from the platen. The configuration of the wafers on the platen is shown in Fig. 1.3. We also need a method a method for indexing the signals, so we can relate the signals to a specific wafer.

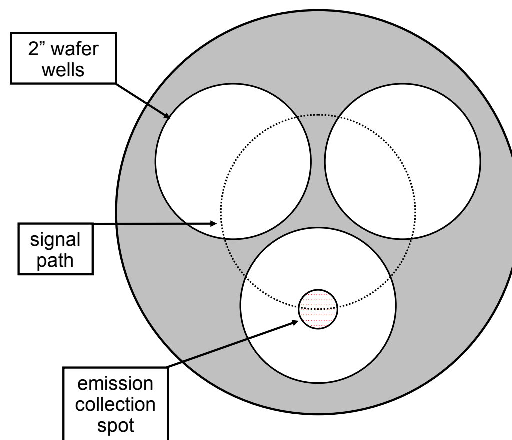

Fig. 1.3. Schematic of D-125 platen, top-view.

The two Sandia Veeco D-125 reactors have somewhat different rotating shaft and platen configurations. Dan Koleske's reactor (DNZ) has a solid rotating shaft machined from a single piece of titanium-zirconium-molybdenum (TZM) alloy. This configuration makes it difficult and relatively expensive to make modifications to DNZ. The end of the DNZ shaft is machined into a conical shape, which mates into a complementary hole in the bottom of the DNZ platen. Andy Allerman's reactor (GNC) has a rotating shaft with a smaller removable tip (referred to as the arbor), which makes reactor modifications somewhat easier. For this reason we originally targeted GNC for the UVV-ECP installation. The bottom of the GNC platen has a small protruding cone which mates into a cup at the end of the arbor.

In both GNC and DNZ the platen is actually free to rotate about the shaft, with only friction preventing this movement. During rapid deceleration/acceleration this slippage can be rather severe and is easily observable. The amount of slippage (if any) occurring at steady state conditions is unknown. Platen-shaft slippage creates a non-trivial signal synchronization and indexing problem. We needed to develop a method of preventing this free rotation, while still allowing for easy loading and removal of the platen (the wafer loading procedure involves transferring the entire platen from the load-lock to the reactor chamber). Our first prototype was a relatively simple modification to the GNC hardware. A slot was cut into the cone protruding from the bottom of the GNC platen. A hole was drilled across the end of the arbor cup, and a 30 mil molybdenum wire was threaded through it. The wire served as a pin that mated into the platen-cone slot. This hardware was tested on a benchtop mockup outside of the reactor. As expected, the pin-and-slot configuration prevented slippage. However, during acceleration and deceleration some increased degree of platen wobble was observed. This motion is probably due to the off-axis torque created by the pin-slot contact. At constant rotation speed the amount of wobble (verified with alignment laser) was very small, and normally no greater than the amount observed without the pin-and-slot configuration.

With the platen no longer free to rotate with respect to the main shaft, we can attach an encoding mechanism to the portion of the shaft that protrudes outside the reactor chamber. A small external synchronization wheel (ESW) was fabricated and mounted to the end of the rotating shaft (in the laboratory mockup). The ESW has three equally space slots that correspond to wafer locations on the platen. A single smaller notch was also machined on the edge of the ESW. These slots are probed with OMRON photomicrosensors, which give a TTL ON signal when a slot is in the field of view. The signals from the photomicrosensors are shown in Fig 1.4. The signal from the three equally spaced slots is referred to as the Gate Signal, and the signal from the smaller slot is referred to as the Hardware Trigger. When the ESW is properly aligned with respect to the platen, a high Gate Signal means we are viewing a wafer. The sequence of the Gate Signal with respect to the Hardware Trigger provides the indexing; in other words it let's us know which wafer we are looking at.

Another factor to be considered is the duty cycle of the Gate Signal. The fraction of the signal path in Fig. 1.4 that intersects the three wafers is equal to 0.80. However, we cannot use an 80/20 duty cycle (80% on, 20% off) because of the finite size of the emission (and reflectance) collection spot. The effect of the spot size is illustrated in the idealized R(550) curve in Fig. 1.4. This is the expected reflectance signal at 550 nm when three specular wafers are loaded on the platen. The platen is a diffuse reflector, so it yield a near zero signal. When the collection spot is entirely on the wafer we get a constant signal. The trapezoidal shape of the waveform is produced when the collection spot overlaps the wafer and platen. In order ensure we only detect signal when our collection area (~14 mm diameter) is **entirely** on a wafer we

must use a ~55/45 duty cycle (instead of 80/20). The Gate Signal in Fig. 1.4 illustrates a 55/45 duty cycle.

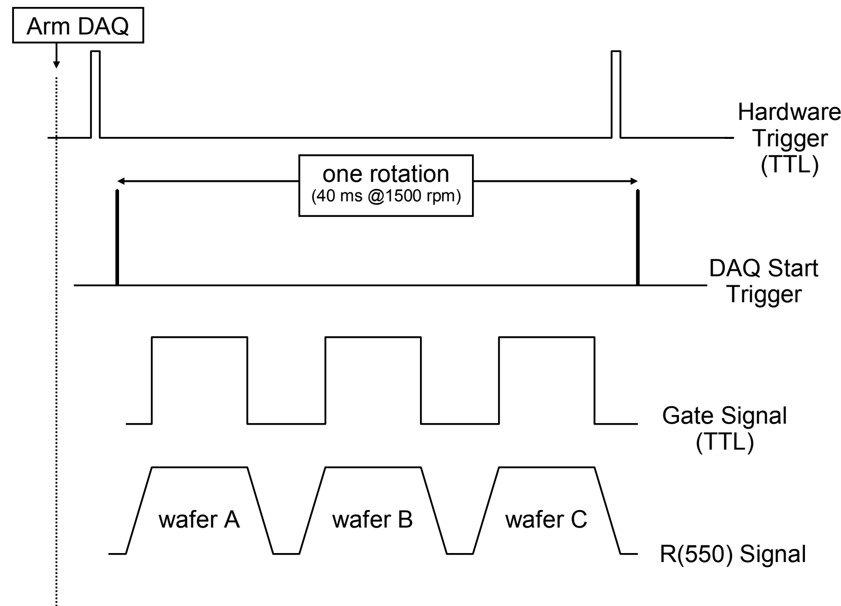

Fig. 1.4. Timing diagram (shutter open).

The 55/45 duty cycle means we are loosing almost factor of 2 in signal collection time relative to our single wafer MOCVD system. Combined with the 2.6 X loss in optical throughput described in Section 1.1, we have lost a factor of 4.7 X by going to the D-125 system. This also assumes we have three equivalent wafers loaded and are able to signal average all wafers. If we choose to examine only one wafer, we loose another factor of 3.

1.4 The Data Acquisition System

A standard Windows-based Dell PC was used as the data acquisition (DAQ) platform. A National Instruments (NI) PCI-6602 high-speed counter/timer board was used to collect the TTL signals from the two photomicrosensors (Gate and Trigger) and the 405 nm signal from the pulse-counting photomultiplier tube (PMT). A National Instruments PCI-MIO-16XE-10 multifunction board was used to gather analog signals and control the shutter that modulates the reflectance signal (see Fig. 1.5).

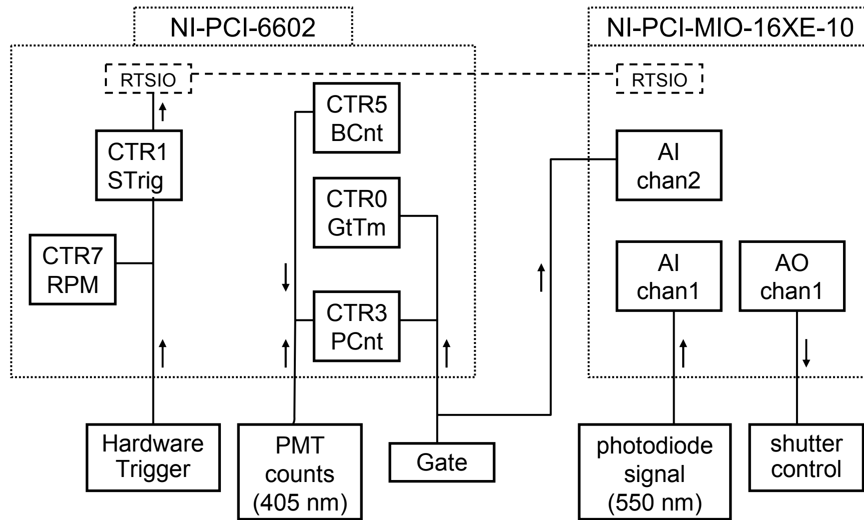

Fig. 1.5. DAQ schematic.

The DAQ code was written in Visual Basic and made considerable use of NI-ComponentWorks controls, graphics, and DAQ objects. One major hurdle in developing this application was maintaining a high software duty cycle efficiency. The total software overhead time (e.g. configuring DAQ boards, reading board signals, number crunching, updating graphics, saving data) needs to be small compared to data collection time. The minimum time to perform a complete DAQ software cycle was empirically determined to be in the 50-100 ms range. One platen rotation at 1500 rpm takes 40 ms (see Fig. 1.4). If we wrote the code to collect and analyze the signal after only one rotation we would miss the next 2 or 3 rotations due to the software overhead time, yielding a duty cycle efficiency of 25-33%. We need a method of collecting data uninterrupted over multiple rotations (e.g. >10), which involve buffering the intermediate output. This is rather easy for the analog input (550 nm data) because the multifunction board is typically used to collect an uninterrupted data stream. Setting up the PCI-6602 counting board proved to be more difficult.

The asynchronous pulse train from the PMT is wired to the source pin on Counter 3 (CTR3-PCnt) and the Gate Signal from the ESW is wired to the CTR3 gate. We would like the CTR3 to begin counting on the leading edge of Gate Signal (see Fig. 1.4), stop counting on the falling edge, store the count value in a buffer, and then repeat for N cycles. Note that with this method we are integrating the 405 nm signal over a wafer. We originally thought the NI application method "Buffered Event Counting" would do exactly this, but it unfortunately does not stop the counter at the falling edge of Gate Signal (it stops at the next leading edge). After considerable angst we found another NI application method called "Buffered Pulse-Width Measurement" that does the trick. As used in this application the nomenclature of this method is rather confusing. Normally for this method a synchronous pulse train of known frequency would be wired to the counter source, and the pulse to be measured (for its pulse width) would be wired to the counter gate. The number of counts measured while the counter gate was high would be a measure of the gate pulse width. So as normally used this method has the unknown signal (to be measured) wired to the gate, and the known (or control) signal wired to counter source. For our

application we have the situation reversed, which is why the nomenclature is confusing. We wire the control signal (Gate Signal) to the counter gate, and wire the signal to be measured to the source.

One idiosyncrasy of the Buffered Pulse-Width Measurement application method is that there must be at least one count at the source when the gate is high, otherwise an error occurs. When the platen is at low temperature and the reflectance signal is modulated off, the PMT output signal is just its dark count rate of 20-50 cps. This is not enough to ensure at least one count will appear. So we generate a background pulse train (BCnt) of known frequency using CTR5 and combine this with the PMT signal (see Fig. 1.5). BCnt is typically set at 300 Hz, and is simply subtracted from each measurement by the software.

The Gate Signal is also wired in parallel to CTR5 in order to measure its pulse width (GtTm). In this case we use the Buffered Pulse-Width Measurement application method in the mode it was intended. So we get a corresponding measurement of the GtTm for each measurement of the number of counts (PCnt). The light intensity is proportional to the actual count **rate,** which is equal to (PCnt-BCnt)/GtTm.

The Hardware Trigger (see Fig. 1.4) from the ESW is wired to two counters; CTR7 and CTR1 (see Fig. 1.5). A simple Single-Period Measurement application method is used with CTR7 in order to measure the platen rotation rate (RPM). This measurement is used to determine the time scale of the analog measurements (AI-chan1 and AI-chan2) for the next DAQ cycle. The RPM is also displayed so the MOCVD operator has a direct and absolute measurement of the spin rate. The Hardware Trigger is also wired to CTR1, which is used to generate the DAQ Start Trigger (STrig, see Fig. 1.4 and 1.5). The analog input device (AI) on the multifunction board senses the DAQ Start Trigger over the Real-Time System Integration (RTSI) bus and begins data acquisition. The two main input counters (CTR0, CTR3) also wait until they see STrig, ensuring that the 405 nm and 550 nm signals are properly synchronized. It is possible to program a delay between the Hardware Trigger and the DAQ Start Trigger in case the physical location of the Hardware Trigger photomicrosensor is not ideal.

The flow of the DAQ software is shown schematically in Fig 1.6. After the system is initialized, all input devices are configured and armed. This involves setting up the number of measurements to be collected by CTR3 (PCnt) and CTR0 (GtTm). The number of measurements is simply three (3 wafers/rev) times the number of platen revolutions (N-rev) we intend to measure (typically 2-30 revolutions, set by the user). The time scale that we program the analog input DAQ (AI) is calculated using N-rev and the rotation speed (RPM). After arming all devices (CTR1-Strig is armed last), the next Hardware Trigger observed activates CTR7 (RPM) and CTR1 (Strig). After a programmable delay (which may be 0 ms) CTR1 produces a Start Trigger that activates CTR3, CTR0, and AI. The analog device (AI) begins collecting data immediately at a predetermined frequency and for a predetermined time. CTR3 (PCnt) and CTR0 (GtTm) begin counting at the next leading edge of the Gate Signal. The software then waits for all 4 input devices to finish, which they signify by firing an AcquiredData event. The CTR7 (RPM) should always finish first because it only requires one platen revolution.

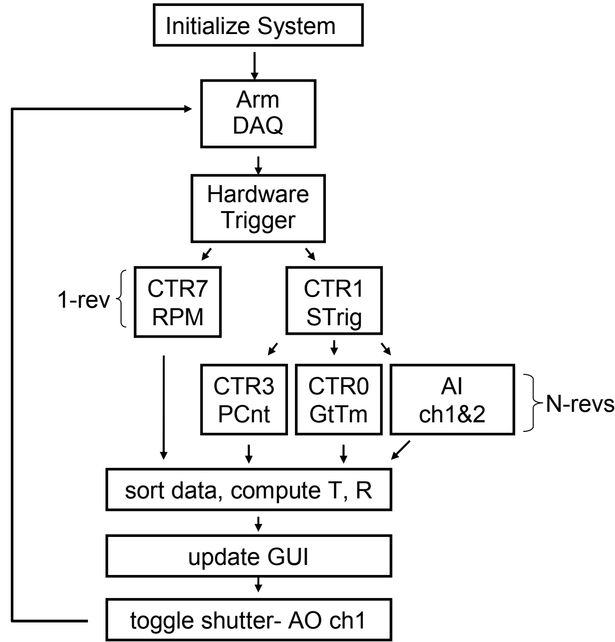

Fig. 1.6. Software Flow Diagram.

After all events have fired the data is sorted, averaged, and assigned to a specific wafer. For the 550 nm signal the analog waveform of the Gate Signal (AI-chan2) is used to sort and index the data from AI-Chan1. Next, the graphical-user interface (GUI) is updated, and the light injection shutter is toggled (if open-close it, if closed-open it). Then the entire sequence is repeated until user intervention stops the program (future versions may run for a predetermined time period).

In order to compute the emissivity-corrected temperature we need to know the reflectance. In order to compute the reflectance from a hot surface, we have to make two measurements. One measurement is with the light injection shutter closed, which yields the raw thermal emission signal (E_r). The next measurement is with the shutter open, which yields the sum (Σ_r) of the raw reflectance signal (R_r) and thermal emission signal; $\Sigma_r = E_r + R_r$. From these two measurements we extract R_r, which is then used to compute the absolute reflectance. The emissivity (ε) for an opaque material is simply given by $\varepsilon = 1 - R$. Using this value and the calibration curve (e.g. Fig. 1.2) we can compute the absolute temperature (we also need to account for window transmission). The net effect of this procedure is that we need two DAQ cycles (Fig. 1.6) in order to compute T and R. We also need to remain cognizant of the time difference between the E_r and Σ_r measurement.

One problem with the multiwafer DAQ system is the user can quickly be overwhelmed by the amount of data collected. For the single wafer system we were able to display all relevant data in one frame (or window). Now, given the increased amount of data we decided to split the GUI into 5 frames. Two frames deal with setting up the program (Control Panel) and examining the raw signals (Raw Signals), and are shown in Fig. 1.7. The upper right hand corner of Fig. 1.7 shows the analog Gate Signal (blue) and raw 550 nm reflectance signal (green/red) for 3 platen rotations. In this example there are 3 unique wafers loaded in the platen. Each wafer has its own GUI frame (not shown) that displays the R and T data at 405 and 550 nm, giving a total of 4 graphs per wafer.

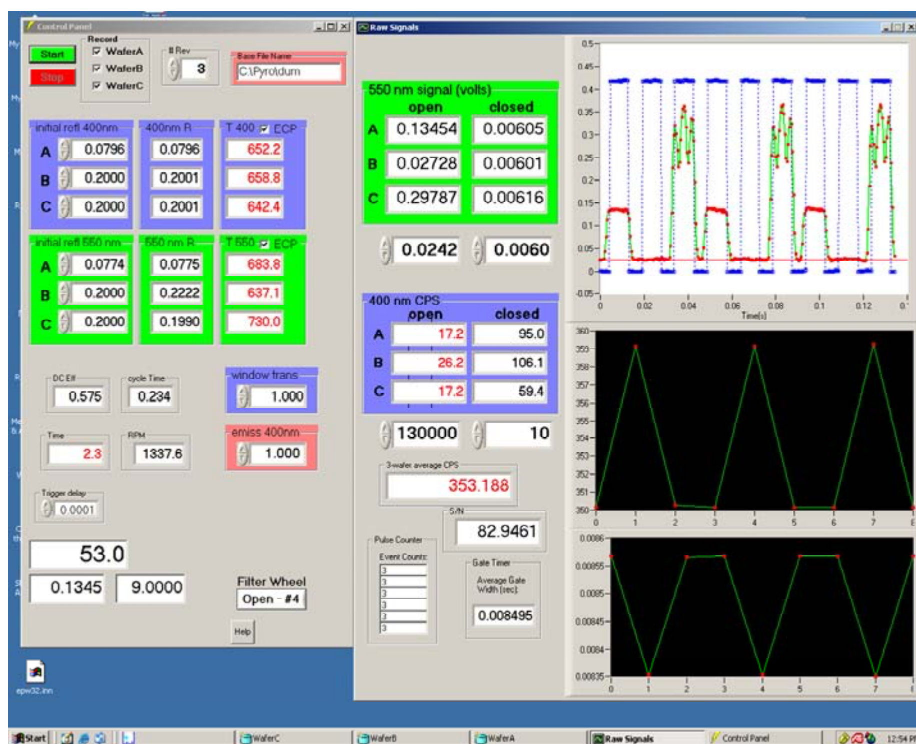

Fig. 1.7 Two frames of the GUI; Control Panel and Raw Signals.

1.5 System Performance

The prototype system was extensively tested in the spring of 2004 and found to perform in line with expectations. The plan was to install the system on the GNC MOCVD platform in the summer of 2004 during a maintenance cycle. This would entail replacing the existing arbor with the modified version containing the molybdenum pin. Unfortunately, when we opened the reaction chamber we found that the arbor was frozen to the main shaft and could not be removed. This setback, and other programmatic needs forced us to postpone the UVV-ECP installation into FY2005. We document the performance of the prototype so it can be used as a baseline to compare with future performance. It is likely that some unforeseen reactor hardware problems will crop up in the future, but we expect the fundamental performance properties of the UVV-ECP prototype to be maintained (e.g. software duty-cycle efficiency, and S/N).

The dependence of the software duty-cycle efficiency on N-rev (at 1500 rpm) is shown in Table 1.1. As expected, as N-rev is increased the efficiency generally increases because the software overhead time becomes a smaller fraction of the total scan cycle time. The scan cycle time is the total time it takes to make one loop in Fig. 1.6. The good news is we can achieve efficiencies of 0.8-0.9 with reasonable N-rev values (7-20). For situations where the temperature or reflectance is changing rapidly we need to minimize N-rev (and the scan time) to avoid phase lag effects between the E_r and S_r measurements (see previous section), with the tradeoff being efficiency. For N-rev = 4 we can still achieve an efficiency of 0.68.

Table 1.1. Software duty-cycle efficiency at 1500 rpm.

N-rev	Software efficiency	Scan cycle time (sec)
3	0.51	0.234
4	0.68	0.234
6	0.70	0.344
7	0.82	0.344
11	0.78	0.562
12	0.85	0.562
18	0.92	0.783

The most important metrics of the system are the signal-to-noise ratios (S/N) for the temperature and reflectance measurements. For the 405 nm channel we are using pulse-counting electronics which is expect to yield shot-noise limited signals. For a given count rate (I) and counting time (τ) it is easy to calculate the expected S/N; $S/N_{rms} = (I\tau)^{1/2}$. For the 405 nm reflectance channel we have abundant signal, in fact we normally attenuate the light source to yield 1-4 MHz count rate for a sapphire wafer (We limit the maximum count rate to less than 10 MHz because of non-linearities that occur in the PMT and pulse counting electronics at very high count rates). For the benchtop prototype running at 1500 rpm we have measured S/N_{rms} and compared this to the theoretical value (see Table 1.2). The measurements are from one sapphire wafer with the raw reflectance signal set at 1 MHz. The noise on the 550 nm analog signal is often determined by intrinsic amplifier noise and stray 60 Hz noise, which makes it difficult to calculate *a priori*. Measurements for the 550 nm channel are also shown in Table 1.2.

Table 1.2. S/N measurements for 405 nm and 550 nm reflectance.

N-rev	Measured S/N (405 nm)	Theoretical S/N (405 nm)	Measured S/N (550 nm)
4	150	170	310
18	320	370	950

Notice that the measured and theoretical S/N values for the 405 nm channel are in reasonably good agreement. A S/N of 200-400 should be adequate for most applications, but it considerably less than the performance of our single-wafer system [e.g. S/N(405 nm) ~ 10^3, S/N(550 nm) ~ 10^4, ~ 1 Hz bandwidth]. Recall that we are loosing integration time due to the 55% duty cycle on the Gate Signal, and another factor of three when we measure only one wafer in the platen. These two factors alone reduce the 405 nm S/N by a factor of 2.3 X. For the 405 nm channel we can easily dial up the initial reflectance signal to 2 MHz, and if we also measure and average 3 wafers we would regain a total factor of $(6)^{1/2}$ = 2.45 X. Also, the reflectance of

GaN is higher than sapphire (0.2 vs. 0.08), so this should give us an additional factor of ~ 1.6 X. So it appears we can achieve a 405 nm S/N of ~ 10^3 for many circumstances (~0.6 Hz bandwidth). We cannot arbitrarily increase the reflectance signal for the 550 nm channel, but by averaging 3 wafers and accounting for the higher GaN reflectance we can reasonably expect to achieve a S/N of 2-3 X 10^3.

We could not heat the platen on the benchtop prototype, but by using the measured blackbody calibration curve (Fig. 1.2) and the known characteristics of the system we can calculate the expected temperature noise. The calibration data shown in Fig.1.2 is fit very well using the Planck radiation distribution function (solid curves) [3]. In the Wein limit the distribution function reduces to Eqn. 1.1. Differential analysis of Eq. 1.1 allows us to derive the approximate temperature noise (ΔT_{rms}), which is given in Eq. 1.2. This curve is plotted in Fig. 1.8 for the following conditions; ε = 0.8 (GaN value), 3-wafer average, scan cycle time = 1 sec. For these conditions the actual counting time (τ) is equal to 0.52 seconds (after accounting for the Gate Signal duty cycle and software efficiency). We also use a typical window transmission of 0.92. For a one-wafer measurement the temperature noise will be √3 larger.

$$S(counts) = A \cdot \varepsilon \cdot \tau \cdot \exp\left(-\frac{c_2}{\lambda T}\right) \qquad (1.1)$$

A = blackbody calibration factor

ε = emissivity

τ = counting time

c_2 = 1.438 X 10^7 nm-deg (2nd radiation constant)

λ = effective wavelength

$$\Delta T_{rms} \approx \frac{\lambda T^2}{c_2}\sqrt{\frac{\exp(c_2/\lambda T)}{A \cdot \varepsilon \cdot \tau}} \qquad (1.2)$$

Note that above 1000°C (typical GaN conditions) the temperature noise is well below 0.1°C, which is certainly adequate performance. As the temperature is lowered into the 700-800°C range the temperature noise starts to become significant. This is the temperature range for InGaN alloy deposition, and here the performance of the pyrometer becomes critical. The InGaN emission wavelength has a temperature sensitivity of 1-2 nm/deg, so temperature uncertainties and drift are very important for reproducibility. Near 800°C the system should be useful using a counting time of a few seconds, but near 700°C we may need to time average over 10's of seconds. In the future we will search for ways of improving S/N, such as increasing the effective wavelength.

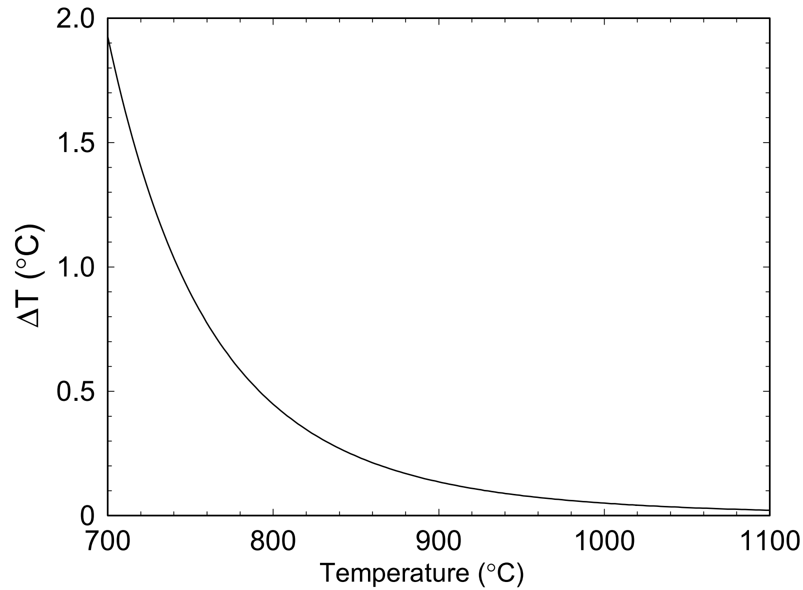

Fig. 1.8. Temperature noise (rms) for 1 second scan cycle time, 3-wafer average.

1.6 References

1. J.A. Simmons et al, “Final Report on Grand Challenge LDRD Project: A Revolution in Lighting-Building the Science and Technology Base for Ultra-Efficient Solid State Lighting”, Technical Report, Sandia National Laboratories, Albuquerque, NM 87185, SAND2004-2365.

2. W.G. Breiland, “Reflectance-Correcting Pyrometry in Thin Film Deposition Applications”, Technical Report, Sandia National Laboratories, Albuquerque, NM 87185, SAND2003-1868.

3. D.P. DeWitt and G.D. Nutter, eds. “Theory and Practice of Radiation Thermometry”, John Wiley and Sons, Inc. 1988.

2 Reproducible Magnesium Doping (J.R. Creighton, G.T. Wang)

2.1 Introduction

Magnesium serves as the dominant p-type dopant for GaN and its alloys, and is typically delivered during MOCVD via the organometallic precursor magnesocene ($MgCp_2$, Cp = cyclopentadienyl). Unfortunately, to date controlled incorporation of Mg into III-nitride films via MOCVD has not been without serious problems. The result is often unpredictable Mg concentration profiles that may greatly vary after the reactor has been perturbed (e.g. from any repair) or even from run-to-run, as has been observed in our research GaN MOCVD systems. Even in reactors in which the Mg doping process is largely reproducible, the Mg profile in the grown films is marked by long transients corresponding to the turn-on and turn off of the doping process. This issue, sometimes referred to as a Mg "memory effect," is problematic since sharp doping profiles are required for optimal device performance.

We previously examined the interaction between $MgCp_2$ and NH_3 at typical III-nitride reactor inlet conditions in order to improve our understanding of Mg incorporation issues [1,2]. This work was the first in-depth investigation of the reaction between $MgCp_2$ and NH_3, and was performed using a joint experimental and theoretical approach. Our results demonstrated that complexation reactions between $MgCp_2$ and NH_3 are very likely responsible for the Mg doping "memory effects" and erratic incorporation problems. These reactions may produce both a 1:1 adduct; $Cp_2Mg{:}NH_3$, and a 2:1 adduct; $Cp_2Mg({:}NH_3)_2$, both of which have very low vapor pressures (<< 1 mTorr). Condensation of these adducts on the reactor walls, as well as homogeneous nucleation of crystalline adduct could effectively remove the Mg precursor from the gas stream. The reactions were totally reversible, suggesting we were dealing with equilibrium phenomenon, as in Eqs. 2.1 and 2.2

$Cp_2Mg + NH_3 \leftrightarrow Cp_2Mg{:}NH_3$ (1:1 adduct) (2.1)

$Cp_2Mg{:}NH_3 + NH_3 \leftrightarrow Cp_2Mg(NH_3)_2$ (2:1 adduct) (2.2)

$$K_p = \frac{P(MgCp_2(NH_3)_2)}{P(MgCp_2)P^2(NH_3)} \qquad (2.3)$$

In our previous work (FY2003), preliminary evidence suggested that heating the gas mixtures to the 50-100°C range could shift the equilibrium back towards the unassociated reactants and prevent adduct condensation. This is shown schematically with the phase diagram in Fig. 2.1. Low temperatures and/or high reactant concentrations favor adduct formation, and as soon as the adduct partial pressure becomes equal to its vapor pressure condensation will occur (upper right-hand corner of Fig. 2.1). This boundary is defined by the equilibrium constant (Eqn. 2.3) and the adduct vapor pressure (P^v), and is given by the ratio P^v/K_p. The preliminary work was performed in a flow cell where the gases were not well mixed. The goal of this task was to measure the condensation phase diagram under well-mixed and reliable conditions that span typical MOCVD inlet conditions.

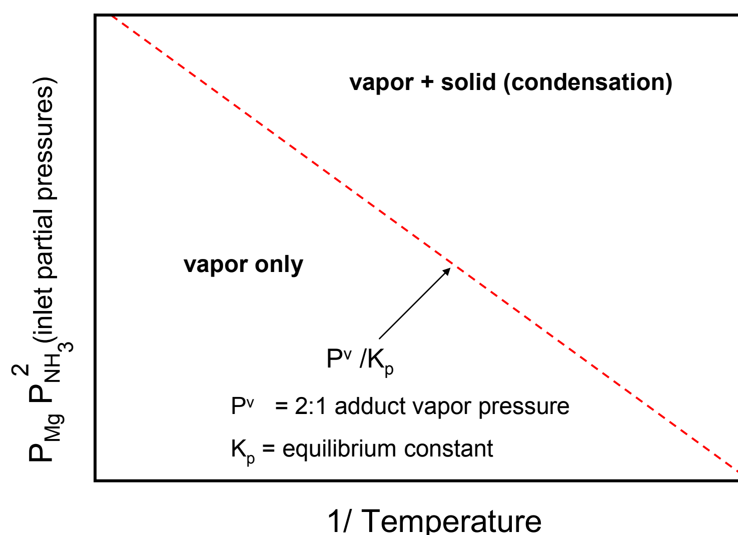

Fig. 2.1 Phase diagram for $MgCp_2$ + NH_3 adduct condensation conditions (NH_3 in excess)

2.2 Experimental

The method used to determine the condensation phase diagram for the $MgCp_2$ + NH_3 is similar to one we previously used to determine the vapor pressures of the TMGa:NH_3 and TMAl:NH_3 adducts [3]. A quartz crystal microbalance (QCM) is used to monitor condensation. However, unlike the TMGa and TMAl work, we need to heat the gas mixtures considerably above room temperature (e.g. 60-120°C). The basic approach is to prepare a gas mixture at concentrations and temperatures just below the condensation boundary. This mixture then flows across the QCM held at a somewhat colder temperature. If the QCM temperature is low enough to place the mixture above the condensation boundary (upper right hand portion of Fig. 2.1), then condensation will occur. Once a specific temperature has been established, the boundary is typically probed by varying the $MgCp_2$ concentration, although in principle it could also be determined by changing the NH_3 concentration. The latter method is more difficult because significant changes in NH_3 concentration can alter the heat transfer of the system, causing the QCM temperature to drift. Some of the major difficulties encountered with this technique are properly mixing the gases without leading to condensation upstream of the QCM, and maintaining the proper temperature gradient in the system. In this study many variations and modifications to the QCM cell were made in an attempt to achieve ideal results. A schematic of the final cell configuration is shown in Fig. 2.2.

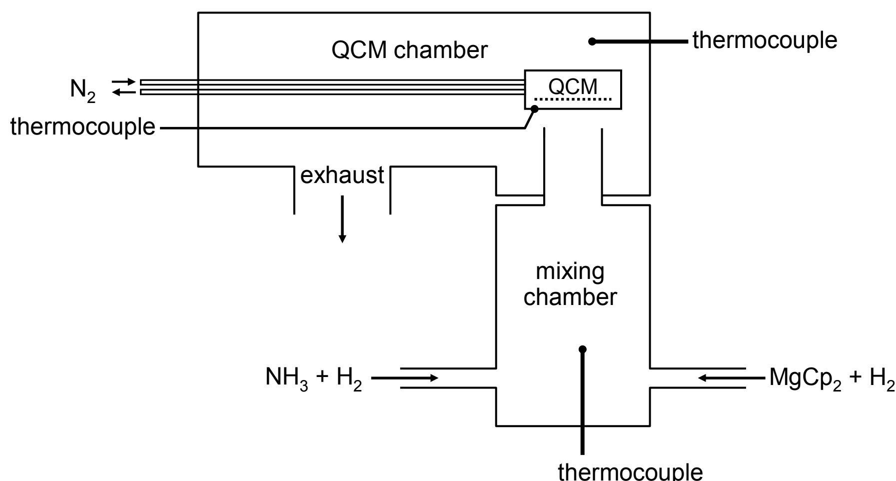

Fig. 2.2 Schematic of QCM cell

Internal thermocouples are used to measure the gas temperature in the mixing chamber and QCM chamber. A thermocouple is also spot-welded to the QCM housing. The two chambers where wrapped with heating tapes and independently heated. The gas inlet lines were also independently heated. Normally, the mixing chamber is set at a temperature 5-10°C above the QCM chamber to provide the needed temperature gradient. A small flow of N_2 gas was also used to cool the QCM another 5-10°C below the QCM chamber gas temperature. The goal is to achieve condensation only on the QCM itself, and not on any upstream or nearby surfaces (condensation will invariably form downstream in the colder exhaust plumbing). Upstream condensation often leads to experimental anomalies and unusual transients and must be avoided.

Partial pressures of NH_3, H_2 and $MgCp_2$ for this experiment were in the same range as those used for GaN MOCVD, although with the smaller cross sectional area of the QCM cell we reduced the total flow rate by ~ 2X. For most experiments a total flow rate of 7 SLM was used. NH_3 flow rate ranged from 500-2000 sccm, but was set at 1000 sccm for most experiments. H_2 flows through the $MgCp_2$ bubbler (set at 18°C) ranged from 0-1000 sccm, with other H_2 flows adjusted to keep a constant total flow rate of 7 SLM. Total pressure was varied from 50-400 torr.

2.3 QCM Results

In our earlier $TMGa:NH_3$ and $TMAl:NH_3$ adduct research we directly determined the threshold condensation flow (F_c) by an iterative brute-force method [3]. For the $MgCp_2$ system this approach was very time consuming and difficult. So we most often used a new extrapolation/interpolation method. In the new method we measure the condensation (or evaporation) rate for a range of $MpCp_2$ flows. An example of this method is shown in Fig. 2.3 (100 torr, 76.0°C, NH_3 = 1000 sccm). As the $MpCp_2$ bubbler flow rate is dropped from 400 sccm to 200 sccm, notice that the slope (or condensation rate) decreases. When the $MgCp_2$ is

turned off, the film slowly evaporates. A plot of the rate as a function of $MgCp_2$ flow is shown in Fig. 2.4, curve (a). By using a linear interpolation we can determine that the threshold condensation flow for this condition is 110 sccm. Another example at different conditions (60 torr, 74.2°C, NH_3 = 700 sccm) is shown by curve (b).

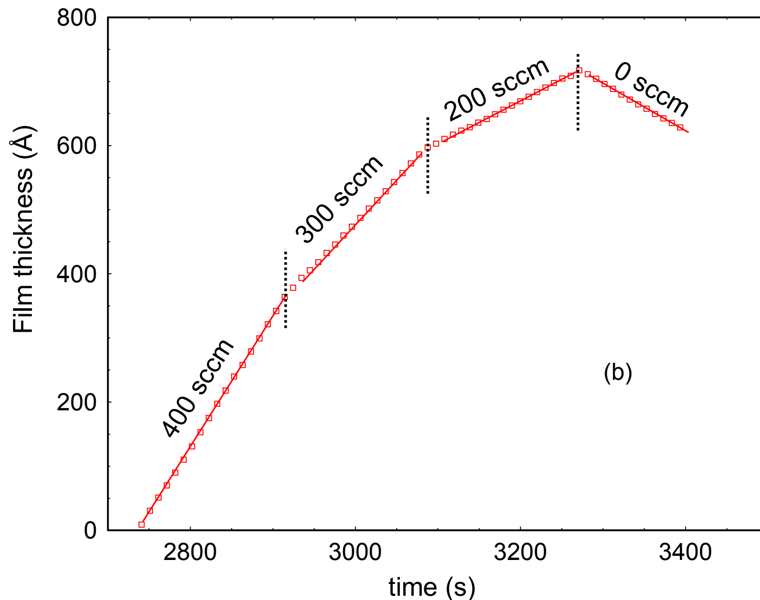

Fig. 2.3 Film buildup at various $MgCp_2$ flow rates

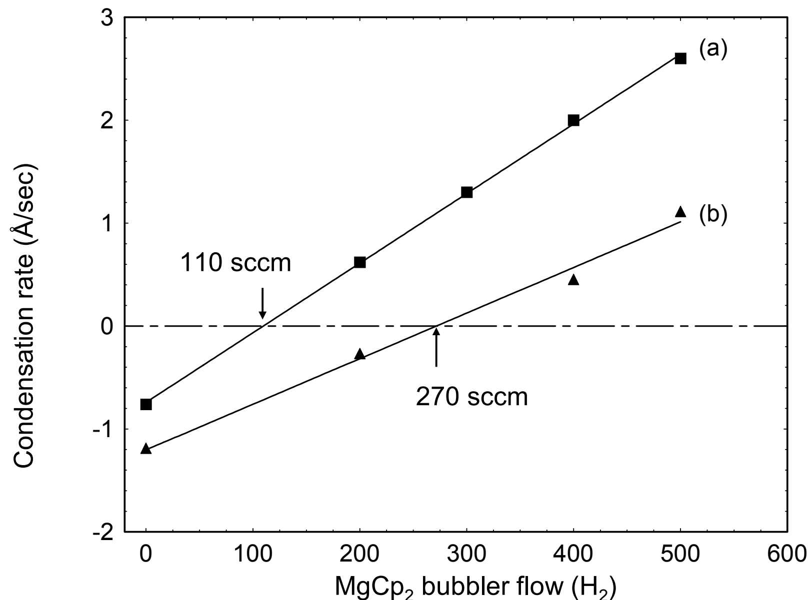

Fig. 2.4 Examples for determining threshold $MgCp_2$ flow

Unfortunately, a significant number of experiments did not yield results as ideal as those shown in Fig. 2.3 and 2.4. Curvature was often seen in the thickness versus time (e.g. Fig. 2.3)

traces, making determination of the condensation and/or evaporation rate problematic. Three possible causes of this behavior are:

1) Upstream or nearby condensation/re-evaporation artifacts
2) QCM temperature drifts (ΔT between crystal holder and actual crystal)
3) Unknown transformation reactions occurring in the film

We originally thought that the poor behavior was due to the upstream artifact (#1 in list). In our earlier work we had solid evidence that upstream deposits could cause some unusual delayed transport effects near room temperature. Numerous cell modifications were made, followed by a complete redesign of the cell (Fig. 2.2). Some improvements in data quality were noted, but by-and-large the problem did not go away. At the higher temperatures (and pressures) tested, we have also found some evidence for a new product being formed (discussed below), and this could be the source of some of the pathological behavior (#3 in above list).

Despite the difficulties, we forged ahead and completed F_c measurements over a temperature range of 65-115°C. In order to span this temperature range, we needed to cover a wide range in concentration. This was mainly accomplished by changing the total pressure (P_t) from 50-400 torr. Recall from Fig. 2.1 and Eq 2.3 that the condensation boundary is given by P^v/K_p. This value is equal to $P(MgCp_2)P(NH_3)^2$, evaluated at experimental F_c values. Results are shown in Fig. 2.5, and include measurements from several versions of the QCM cell. Some scatter is obvious, but overall the quality of the plot is acceptable. Note that the $P(MgCp_2)P(NH_3)^2$ factor spans almost 4-orders of magnitude. Compared to our preliminary results from FY 2003, the condensation boundary is shifted about 15°C to higher temperature. We expected a shift in this direction because the preliminary results were obtained under poorly-mixed conditions where the local NH_3 concentration at the QCM was less than the average cell concentration.

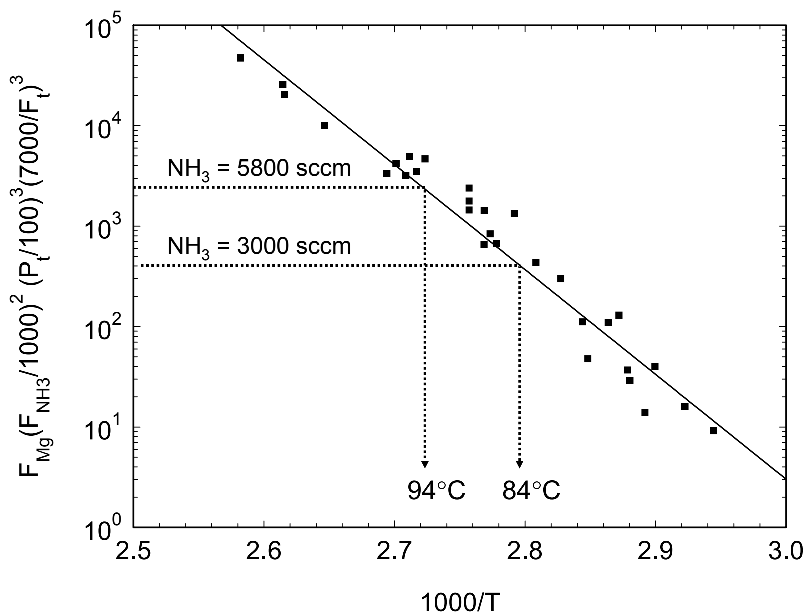

Fig. 2.5 Arrhenius plot of P^v/K_p at threshold flow conditions

Using the new measurements we can compute the minimum temperature needed to prevent condensation at any MOCVD inlet condition. Our normal GaN conditions in our research reactor (CVD1) are; P_t = 140 torr, NH_3 flow = 5800 sccm, H_2 flow = 7600 sccm. Referring to other work, we expect to use a $MgCp_2$ bubbler flow of ~ 200 sccm in order to achieve the desired p-doping levels. For these conditions we need to heat the reactor inlet to at least 94°C (see Fig. 2.5). Heating to this temperature is possible, but it is starting to approach a technically difficult level. Because the boundary depends on $\mathbf{P^2}(NH_3)$, lowering the NH_3 mole fraction has a considerable effect on the temperature requirement. If we lower the NH_3 flow to 3000 sccm (and increase H_2 to 13000 sccm to maintain matched flow conditions) the minimum temperature drops to 84°C (see Fig. 2.5). The boundary also depends on P_t^3, so modest reductions in pressure yield significant reductions in the required temperature. Being able to adjust NH_3 flows and P_t gives us some leeway in the design and operation of the heated injector flange. A method of heating the reactor walls to ~100°C was tested and a heated inlet flange has been designed. Complete system testing will not be complete until FY2005.

One potential pitfall in the heated inlet approach is the possibility that at elevated temperatures some undiscovered irreversible chemical reactions may become viable and lead to the formation of an even lower vapor pressure deposit. Our earlier work near room temperature showed that the $MgCp_2$ reactions (Eq 2.1 and 2.2) were entirely reversible and no evidence for other species was found [2]. For much of the work reported here reversibility appears to be maintained. When a thick deposit of the 2:1 adduct (1000's of Å) is formed and the NH_3 flow is turned off, the entire deposit will normally disappear very quickly (typically in a few seconds) due to the dissociation of the adduct. However, during some experiments a fraction of the deposit was left behind after the initial rapid depletion stage. We originally interpreted this behavior as due to the presence of an upstream or nearby deposit providing a residual NH_3 background pressure that impeded the dissociation reaction. However, the lifetime of the "tenacious" deposit usually far exceeded what we thought was reasonable for the residual NH_3 mechanism. Formation of the new product appeared to correlate with higher temperatures, but the correlation was not perfect. Once formed, we could often remove the deposit by reaction with TMAl, but this procedure did not always work, suggesting that there may be more than one type of new product being formed. It remains to be seen if the formation of the new product(s) will prevent successful Mg doping using the heated inlet approach. If the new product first requires the condensation of the 2:1 adduct (a likely scenario), then the phase boundary we measured (Fig. 2.5) will still be a valid guide.

As a final note, we revisit the physical meaning of the phase boundary. The apparent activation energy (E_a) of the boundary in Fig. 2.5 is equal to 47.8 ± 2.9 kcal/mole (± 2σ). The boundary is defined by P^v/K_p, so $E_a = \Delta H_v - \Delta H_r$, where ΔH_v = 2:1 adduct heat of vaporization and ΔH_r = 2:1 adduct heat of reaction. In earlier work we used density functional theory (DFT) to calculated ΔH_r, which varied from -25.3 kcal/mol to -13.2 kcal/mol, depending on the level of theory. Using these numbers we determine that the 2:1 adduct heat of vaporization (ΔH_v) is in the range of 22-38 kcal/mol (including experimental uncertainties). For reference, the $MgCp_2$ precursor ΔH_v is ~ 16 kcal/mol. We know that the 2:1 adduct has a much lower vapor pressure than the $MgCp_2$, so values of $\Delta H_v \geq 22$ kcal/mol are in line with expectations.

2.4 References

1. J.A. Simmons et al, “Final Report on Grand Challenge LDRD Project: A Revolution in Lighting-Building the Science and Technology Base for Ultra-Efficient Solid State Lighting”, Technical Report, Sandia National Laboratories, Albuquerque, NM 87185, SAND2004-2365.

2. G.T. Wang and J.R. Creighton, “Complex Formation between Magnesocene ($MgCp_2$) and NH_3: Implications for p-Type Doping of Group III Nitrides and Mg Memory Effect”, J. Phys. Chem. A., 108 (2004) 4873.

3. J.R. Creighton, “Vapor Pressures of the Adducts Formed during AlGaN Organometallic Vapor-Phase Epitaxy”, J. Electron. Mater., 31 (2002) 1387.

3 Understanding and Improving GaN growth on Sapphire (D. D. Koleske, M. E. Coltrin, S. R. Lee, D. M. Follstaedt, A. A. Allerman, M. J. Russell, K. C. Cross, C. C. Mitchell)

3.1 Reducing dislocation density of GaN films on sapphire

In FY2004, a new commercial Veeco reactor was installed and qualified. After the reactor was qualified, growth experiments were conducted to improve the GaN film quality on sapphire using a delayed recovery technique. The delayed recovery growth conditions favor the formation of large GaN nuclei on the surface followed by promoting lateral growth to bend dislocations near the sapphire GaN interface. Using this growth technique, the dislocation densities determined from x-ray diffraction were reduced from $2x10^9$ cm^{-2} to $4x10^8$ cm^{-2} in the new reactor. The reflectance waveforms measured on the new Veeco reactor were similar in appearance to previously measured waveforms on the high speed rotating disk reactor.

One major contributing factor to achieving the lower dislocation densities in the new Veeco reactor was utilizing the measured optical reflectance signal to optimize growth. In Fig. 3.1 are listed various GaN thin films growth attributes that can be determined from the optical reflectance during growth. This includes information on film thicknesses, optical constants, nucleation layer (NL) decomposition, NL roughening, and main layer roughening and uniform-

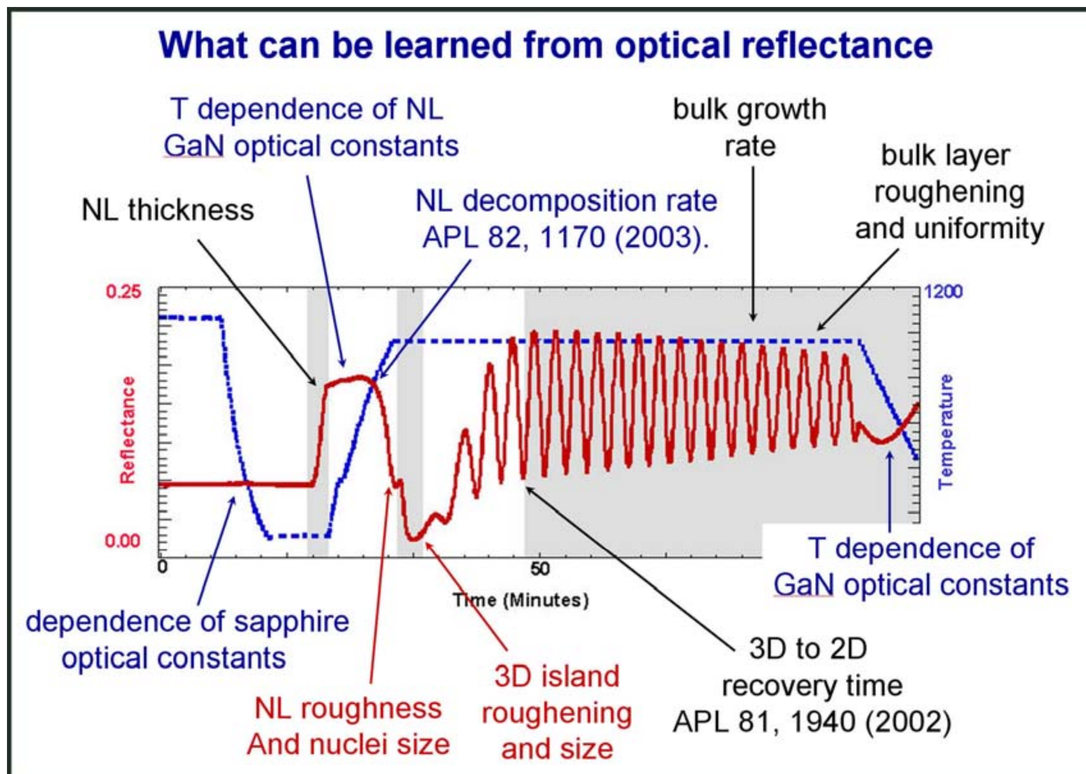

Fig. 3.1. Temperature profile for GaN growth on sapphire shown in blue and optical reflectance waveform measured during growth in red. Various regions of the optical reflectance waveform are highlighted along with the information on the growth that is contained in the waveform.

ity. Publications for this work [1, 2] are listed in Fig. 3.1. In Ref. [1] we used optical reflectance to delayed the 3D to 2D recovery of the GaN films. We also showed in Ref. [1] that the brightness of 380 nm LEDs increased as the 3D to 2D recovery was increased. We quantified the reflectance waveform by defining a term called the recovery time which was the time needed for the reflectance signal to reach 75% of the full GaN reflectance signal near 0.20 [1]. We then showed that as the recovery time for 3D to 2D growth transition was increased the output power of 380 nm LEDs increased. By increasing the 3D to 2D recovery time GaN films with fewer dislocations were grown. Since these dislocations likely act as non-radiative recombination centers their decrease resulted in LEDs with improved light output. In this study the dislocation density was quantified by AFM, where the dislocations appear as pits. Fewer pits were observed in a film with large recovery time compared to a film with shorter recovery time. Because the AFM can only image pure and mixed screw-type dislocations, only a lower bound on the actual dislocation density could be established. From this research it was not clear how general this dislocation reducing technique was or to what extent the 3D to 2D transition could be delayed to achieve lower dislocation densities. In addition, a more rapid-evaluation technique was needed to measure dislocation density to give feed-back for the next growth run.

After the qualification runs were completed in the new Veeco MOCVD reactor, we began to explore growth conditions that delayed the 3D to 2D transition. An additional advantage of the new reactor is the ability to increase the chamber growth pressure to 500 torr, whereas in the older reactor used in Ref. [1] the chamber pressure was limited to 150 torr. By reducing the NH_3 flow rate during the NL annealing and initial high temperature, T, growth stages we were able to increase the 3D to 2D transition time as monitored by the optical reflectance. Concurrently, Stephen R. Lee developed a reciprocal-space model of the Bragg peak widths that describes their dependence on coherence length, tilt variance, and twist variance of a dislocated epitaxial layer [3]. Therefore from measurement of as few as two x-ray reflections the screw and edge dislocation components could be estimated.

In Fig. 3.2, the x-ray ω-scans are shown for the (0004) symmetric reflection and the $(10\bar{1}1)$ out-of-plane reflection for four different GaN films grown on sapphire. Note that as the sample numbers increase from 1-4 the width of the ω-scans increases. For the films shown in Fig. 3.2 decreasing recovery time was used during growth (i.e. going from film 1 to 4) which resulted in the increase in the ω-scan width.

To relate the ω-scan widths to the screw and edge dislocation components the classic formula are used, as discussed in detail in Ref. [3]. Here, we will assume the threads are randomly distributed and the threading dislocation density, ρ, is $\Gamma^2/(4.355b^2)$, where Γ is the measured full width at half maximum (FWHM) of the Bragg peak and, b is the magnitude of the relevant Burgers vector component. The screw component dislocation density, ρ_S, is given by,

$$\rho_S = \left(\frac{10^8}{4.355 b_S^2}\right)\left(\frac{\pi}{180}\right)^2 \omega_S^2 = 260.18 * \omega_S^2, \tag{3.1}$$

and the edge component dislocation density, ρ_E, is given by,

$$\rho_E = \left(\frac{10^8}{4.355 b_E^2}\right)\left(\frac{\pi}{180}\right)^2 \omega_E^2 = 687.79 * \omega_E^2, \tag{3.2}$$

where b_S and b_E are the screw and edge Burger vector components, and ω_S and ω_E are the FWHM of the (0004) and $(10\bar{1}1)$ x-ray reflections measured in degrees.

The dislocation densities using the measured ω_S and ω_E are calculated and plotted in Fig. 3.3 from over 80 GaN films. In Fig. 3.3, the dislocation densities are plotted for GaN films grown

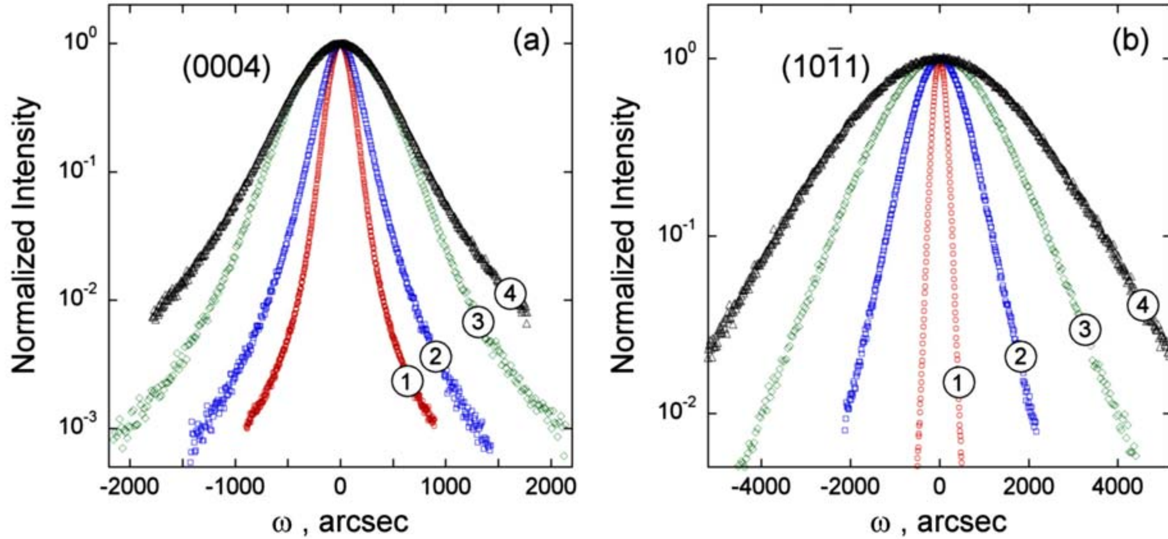

Fig. 3.2. Measured XRD rocking curves from four GaN films grown on sapphire. In (a) the rocking curves are measured around the symmetric (0004) reflection, while in (b) the rocking curves are measured around the skew $(10\bar{1}1)$ reflection. The (0004) reflection provides a measure of dislocations with a screw component and the $(10\bar{1}1)$ reflection provides a measure of dislocations with both screw and edge components.

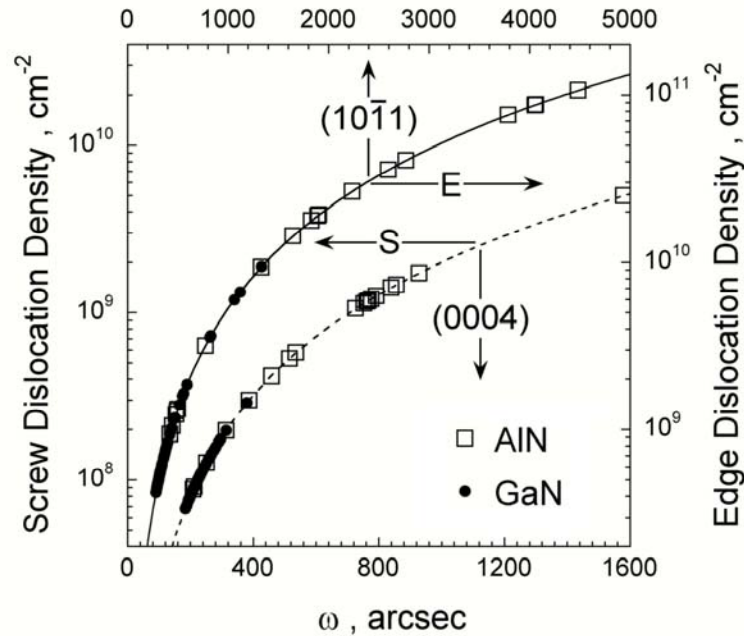

Fig. 3.3. Plot of dislocation density calculated from the x-ray linewidths using Eq. 3.1 and 3.2.

using both GaN and AlN low T NLs. The screw dislocation density is plotted along the left y-axis using the measured ω_S plotted along the lower x-axis and the edge dislocation density is plotted along the right y-axis using the measured ω_E plotted along the upper x-axis. Note that the screw dislocation density is calculated using ω_S following Eq. 3.1 while the edge dislocation density is calculated using ω_E following Eq. 3.2. Since only the screw and edge components are measured, the partitioning between the screw, mixed, and edge dislocation densities is not possible [4], however, based on detailed TEM results approximately 11% of the dislocations are pure screw, 40% are mixed (screw and edge) and 49% are pure edge. As shown in Fig. 3.3, higher dislocation densities (screw and edge component) are achieved when AlN NL are used compared to GaN. Fig. 3.3 also shows that the edge component dislocations are approximately 5 to 10 times larger than screw component dislocations. For simplicity the total dislocation density is often taken as the calculated edge dislocation density.

Although it is well known that narrower x-ray linewidths are a strong indicator of better material quality, previous work on the nitrides have shown that both symmetric and asymmetric reflections are needed to properly assess the GaN material quality. Using x-rays to determine the dislocation density in GaN films has several advantages over other techniques, including being non-destructive, measuring larger (2 mm) regions of the film (unlike TEM which measures only micron sized regions), measuring all of the dislocations in the film volume, and most importantly how rapidly the x-ray reflections can be measured. This last feature is especially important for rapid feed-back for growth optimization.

We used the x-ray technique to measure dislocation density and were able to achieve GaN films on sapphire ranging from 4×10^{8} to 1×10^{11} cm^{-2}. Nomarski images of four selected films are shown in Fig. 3.4, along with reflectance waveform and edge dislocation densities measured from the x-ray linewidths. (Note here that the edge dislocation density is assumed to be equal to the total dislocation density.) The GaN films appear rougher in Nomarski image in Fig. 3.4(a) and the film roughness decreases in Figs. 3.4(b) to 3.4(d). This decrease in the surface roughness correlates to an increase in the dislocation density as listed on the top of each reflectance waveform. The reflectance waveforms also show a decrease in the time it takes for the GaN film to recover to its nominal reflectivity value near 0.20. Previously, we quantified this delay time [1] and from Figs. 3.4(a) to 3.4(d) the delay time decreases dramatically. Although the surface morphology may be rougher in Fig. 4(a) the decreased dislocation density in these films might be advantageous for device structures that are sensitive to higher dislocation densities.

The reason for the increased roughness in Fig. 3.4(a), the increased delay time and the lower dislocation density is because the GaN film shown in Fig. 3.4(a) has a decreased nucleation density and subsequent high T growth on these nuclei favors the formation of hexagonal pyramids as shown in the SEM images in Figs. 3.5(a) and 3.5(b). By favoring this rougher morphology, the dislocations are thought to bend laterally when the growth conditions are changed to enhance lateral growth and promote 2D coalescence. Such a mechanism has been proposed to explain the dislocation reduction during cantilever epitaxy [5] and facet-controlled growth [6]. Dislocations that are not turned at the pyramidal facets, continue to propagate upward to the surface. The propagation of the dislocation up to the surface and bending of the dislocation laterally is shown in the TEM image in Fig. 3.5(c). Here, dislocations that propagate to the surface appear to bunch together in several groups spaced several microns apart marked by a parenthesis in Fig. 3.5(c). Dislocations that bend at the pyramidal facets are also observed to run parallel to the GaN sapphire interface. A more detailed model of GaN grain growth along with comparison and simulation of the reflectance waveforms will be presented in Section 3.3.

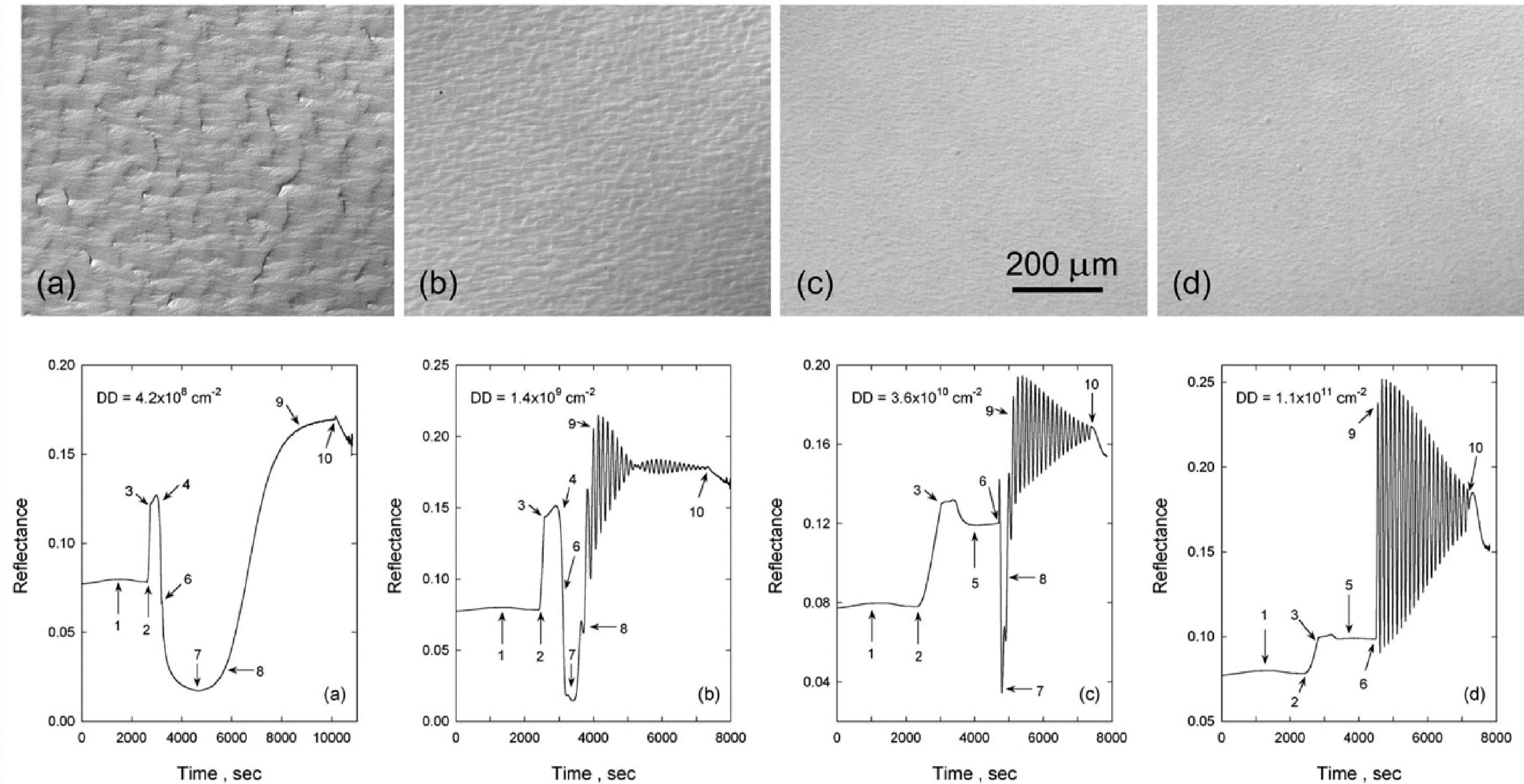

Fig. 3.4 Morphology of the GaN films imaged using Nomarski phase contrast microscopy and the corresponding optical reflectance waveform measured during growth. The corresponding total density is also listed on each reflectance waveform. GaN nucleation layers (NLs) are used in (a) and (b) and AlN NLs are used in (c) and (d). The numbers 1-10 refer to specific growth steps on the reflectance waveforms and are as follows: 1). Sapphire annealing to 1060-1070°C, 2). Start of the NL growth, 3). End of NL growth, 4). Onset of NL decomposition (only for GaN), 5). NL annealing at 1050-1060°C (only for AlN), 6). Beginning of high temperature GaN growth, 7). Minimum in reflectance signal – indicates the point of maximum 3-D roughness, 8) Beginning of the recovery from 3D to 2D morphology, 9) GaN films fully coalesced, 10). End of high T GaN growth.

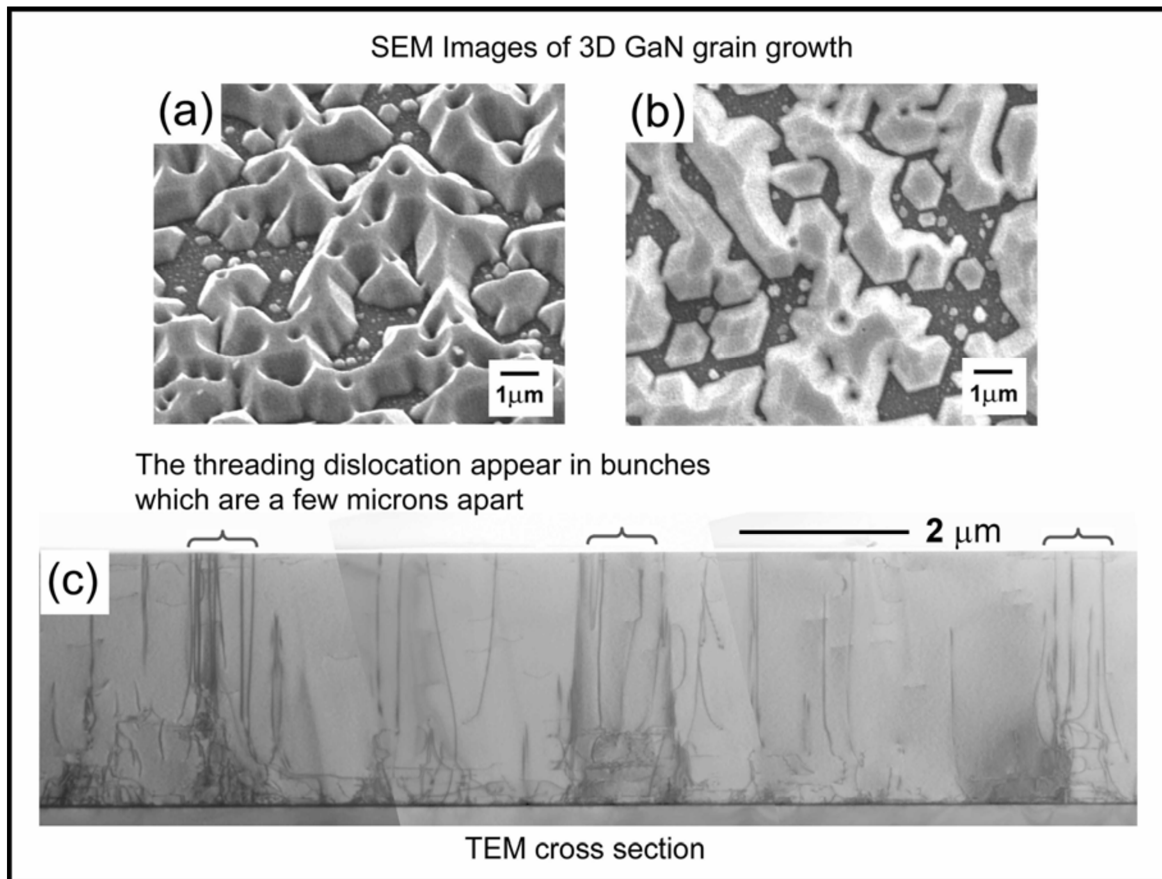

Fig. 3.5. SEM and TEM images of GaN films grown by intentionally delaying the 3D grain to 2D coalescence.

Using the x-ray method to estimate dislocation densities, we have studied how various MOCVD growth conditions influence the dislocation density. Several examples from this study are shown in Fig. 3.6 where the NL thickness was varied and in Fig. 3.7(a) where the initial growth pressure was varied, and in Fig. 3.7(b) where the recovery delay was varied.

In Fig. 3.6, the thickness of the initial GaN or AlN NL was varied and the resulting components of the screw (a) and edge (b) component dislocation density were estimated from Eqs. 3.1 and 3.2. Because other growth conditions in addition to the NL thickness was varied, the solid (GaN NLs) and dashed (AlN NLs) are fits to the lowest dislocation density for each set of films. From Fig. 6, the NL thickness that produces the minimum dislocation density is 15 nm for GaN NLs and between 20 and 30 nm for AlN NLs. Note that a minimum edge dislocation density of 4.2×10^{8} cm^{-2} was achieved using a 15 nm thick GaN NL.

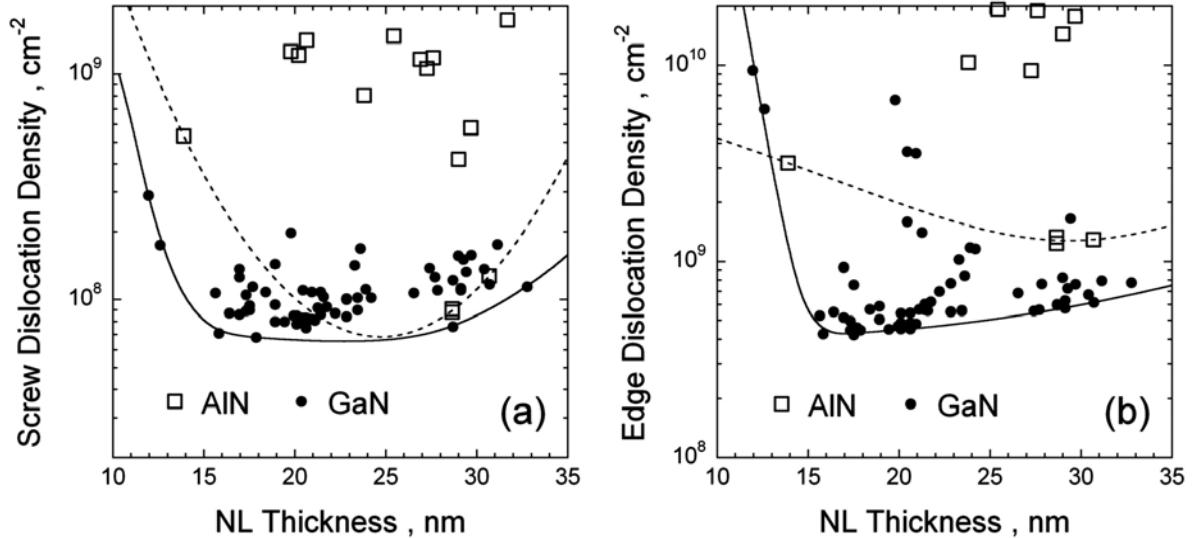

Fig. 3.6. Plots of the (a) screw and (b) edge dislocation density vs. the NL thickness. GaN films grown using AlN NLs are denoted by the open squares and GaN films grown using GaN NLs are denoted by the filled circles. The solid (GaN NLs) and dashed (AlN NLs) lines outline the lower limit of the dislocation density for each NL thickness.

In Fig. 3.7, the influence of two additional growth conditions on the dislocation density was explored for GaN NLs. In Fig. 3.7(a), the initial growth pressure was varied from 50 to 500 torr and the screw and edge component dislocation densities plotted using open squares and filled circles respectively. As in Fig. 3.6, the solid and dashed lines are fits to the minimum dislocations densities at each pressure. From Fig. 3.7(a) it is clear that higher growth pressures produce lower GaN dislocation densities as previously discussed elsewhere [7]. Extending the fits shown in Fig. 3.7(a), dislocation densities below $1x10^8$ cm^{-2} might be expected at a growth pressure of 1600 torr. (This growth pressure can not be reached by the current reactor design). Similar to Fig. 3.7(a), the recovery delay time also influences the resulting dislocation density with increasing recovery delay time producing films with decreasing dislocation densities. For Fig. 3.7(b), all of the data were used for the fits.

In summary the lowest dislocation density films was achieved using 15 nm thick GaN NLs, with initial GaN growth at 500 torr with a recovery delay near 4000 seconds. What is clear from this study is the usefulness of rapid dislocation density determination in these GaN films as well as determining which growth parameters most influence the dislocation density.

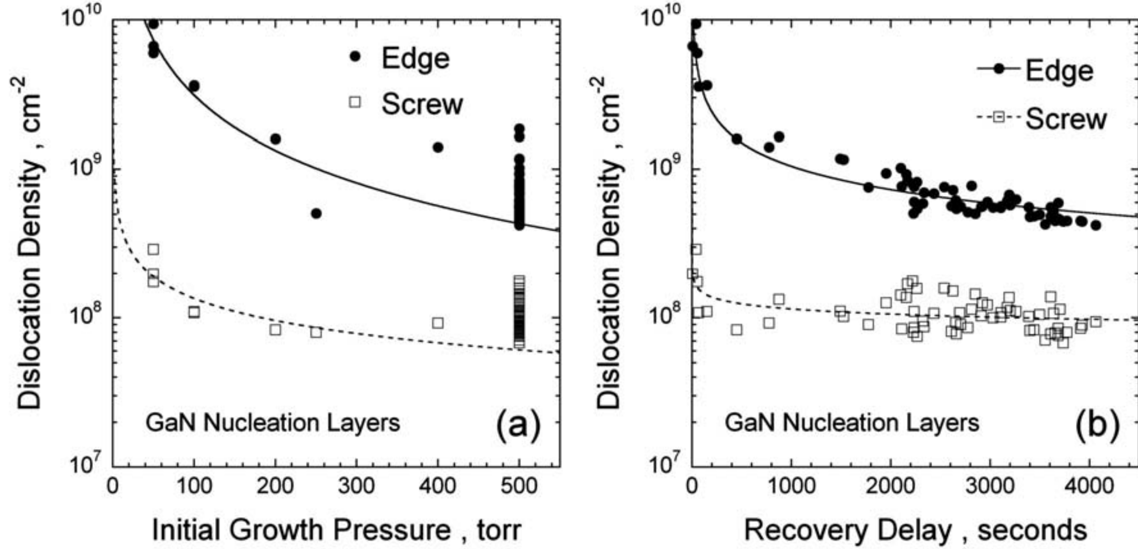

Fig. 3.7. Plots of the screw and edge dislocation components vs. (a) the initial growth pressure and (b) the recovery delay time. The solid and dashed lines are power law fits to the data.

3.2 Nucleation layer decomposition kinetics and nuclei formation

During the ramp from low to high temperature, *T*, GaN nucleation layers (NLs) decompose with the extent of the decomposition depending on annealing conditions [2, 8]. Using normal incidence optical reflectance, the NL decomposition kinetics was measured as a function of *T*, pressure, *P*, and NH_3 and H_2 flow rates. After calibrating the reflectance signal to the NL thickness, the NL decomposition rates were measured and shown to increase with increasing *P* and *T*, and decreasing NH_3 flow. Also, the decomposition rate does not change as the NL growth *T* is varied, but does increase as the NL thickness increases. From the *T* dependence of the decomposition an activation energy, E_A, of 2.7 ± 0.1 eV was measured, while the pre-exponential factor, A_0, depends strongly on the annealing conditions. Fits were developed for the reflectance waveforms as the NL is annealed. The fits include the *T* dependence of indices of refraction and the decomposition kinetics through changes in A_0. Fits are applied to several sets of reflectance waveforms where the annealing conditions were intentionally varied to generate either similar or dissimilar NL decomposition rates.

3.2.1 Fitting the Group III Nitride Reflectance Waveform

This work follows the ground breaking work of Breiland and Killeen who developed a virtual interface method to model normal incidence optical reflectance [9]. With this method the growth rate, *G*, and the high temperature optical constants, *n* and *k*, could be extracted during growth. With this model, simplifying assumptions were made on the range of refraction indices ($n > 4$) and on the adsorbing nature ($k > 0$) of the films and substrates. Using these two simplifying assumptions, a damped cosine expression was derived that was applicable for most semiconductor growth, as shown in Eq. 8 of Ref. [9].

The virtual interface model developed by Breiland and Killeen works especially well when $n < 4$ and the substrate is adsorbing (i.e. $k > 0$). Its applicability for the group III nitrides is problematic because for the wavelengths 400-1000 nm commonly used for reflectance, $k = 0$ for both GaN and sapphire substrate, i.e. they are transparent, $k = 0$. In addition, $n < 4$ for sapphire ($n = 1.77$) and GaN ($n = 2.4$) so the approximation of $n > 4$ can not be used. Finally, GaN films can roughen under certain growth conditions, due to the film growth from discrete grains nucleated on the substrate, and this roughness must be included in many cases in order to get an adequate fit [10]. Here, we calculate the observable real reflectance, $R = |r|^2$, assuming that $n > 1$ and $k = 0$. A detailed derivation is given in Ref. [8] and here we only summarize the final result.

Based on the assumption that both the substrate and film are transparent, k_i and $k_s = 0$, and the various definitions from Eq. 3.6 in Ref. [9], simplify to

$$R_\infty = |r_\infty|^2 = (1 - n_i)^2 / (1 + n_i)^2 ,$$

$$\varphi = \tan^{-1}\left(0 / \left[n_i^2 - 1\right]\right) = 0 ,$$

$$R_i = |r_i|^2 = \left|\sqrt{R_i}\exp(i\sigma)\right|^2 = \left[(n_i - n_s)^2 / (n_i + n_s)^2\right] ,$$

$$\sigma = \tan^{-1}\left[(2(0)) / \left(n_i^2 - n_s^2\right)\right] = 0 , \quad \gamma = 0 , \text{ and } \delta = 4\pi n_i G / \lambda .$$

Above, R_∞ is an optical reflectance term for the film (GaN in this case), while R_i is an optical reflectance term for both the top layer and substrates (GaN and sapphire in this case), where n and k are the real and imaginary optical constants (i.e. $N = n - ik$). The subscripts s and i are subscripts for the virtual substrate (in this case the sapphire substrate) and the internal layer (in this case GaN). The only other term with that is nonzero is δ which is a combination of terms that includes the wavelength of light, λ, and the growth rate, G.

Putting these values into Eq. 6 from Ref. [9], gives

$$R(t) = \frac{R_\infty + R_i - 2\sqrt{R_\infty R_i}\cos(\delta t)}{1 + R_\infty R_i - 2\sqrt{R_\infty R_i}\cos(\delta t)} , \tag{3.3}$$

where t is time and R_∞ and R_i are defined above.

For rough films, the reflected light is attenuated. To model this roughness, the reflectance is multiplied by the term $\exp(-[4\pi\ \sigma(t) / \lambda]^2)$, following Stover [11]. Here, the roughness, $\sigma(t)$, of the film has been assumed to be a function of t. Combining Eq. 3.3 with the roughness attenuation gives

$$R'(t) = R(t) \exp(-[4\pi\ \sigma(t) / \lambda]^2). \tag{3.4}$$

For the 550 nm light typically used, the reflectance attenuation, $R'(t)/R(t)$, is 0.27 for σ of 50 nm, 0.15 for σ of 60 nm, and 0.03 for σ of 80 nm. While Eq. 3.4 adequately describes the roughness attenuation when applied to the thick NL as shown in Fig. 3.8, caution must be used when using it to model roughness, especially when $\sigma << \lambda$. To more accurately model roughness when $\sigma <<$

λ effective-medium methods should be used. In the current paper we will use Eq. 3.3 to model optical roughening, due to its simplicity.

To correlate R to the NL thickness, a thick GaN NL was grown. The optical reflectance measured at both (a) 550 nm and (b) 900 nm for the thick NL is shown in Fig. 3.8. The solid circles denote every tenth measured value of the reflectance signal and the solid lines are fits based on Eqs. 3.3 and 3.4. For the fit, the roughness, ρ, in Eq. 3.4 was assumed to increase linearly in time, i.e. $\sigma = c\ t$. Only c, R_i, R_∞, and δ were varied for the fits.

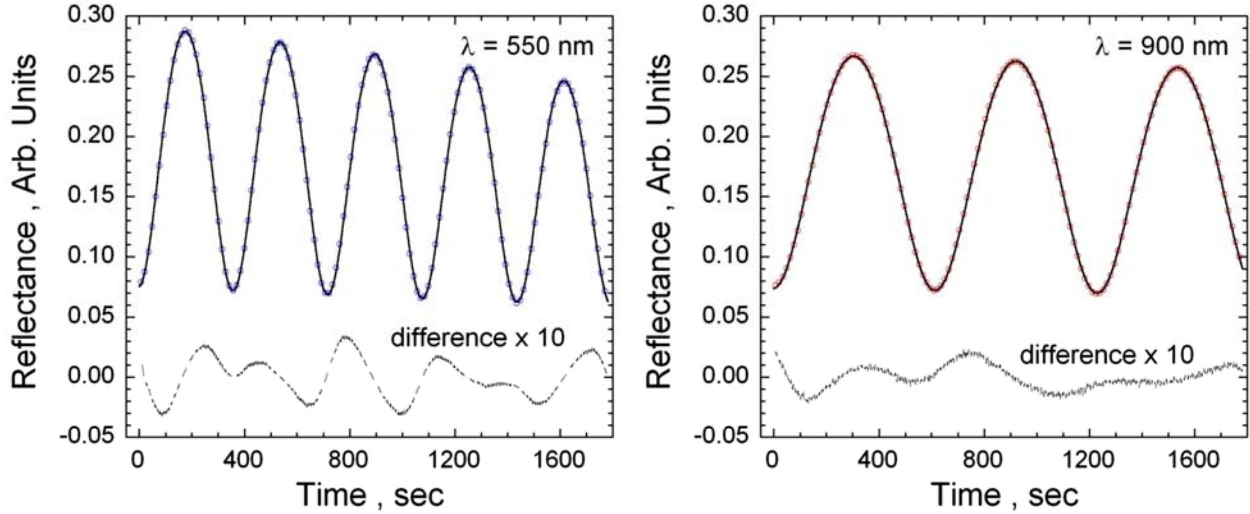

Fig. 3.8. The reflectance waveforms for thick GaN NL are plotted vs. time at wavelengths of (a) 550 nm and (b) 900 nm. Every tenth measured value of the reflectance signal was plotted (solid circles); the solid lines are fits to the data using Eqs. 3.3 and 3.4.

The NL growth rate, G, was calculated using $\delta\lambda /4\pi n_i$ based on the definitions in Eq. 3.1 with $n_i = 2.39$ at $\lambda = 550$ nm and $n_i = 2.32$ at $\lambda = 900$ nm [12]. The calculated G from the reflectance measurements resulted in an average G of 0.317±0.003 nm/s. Note that the NL G is assumed to be constant and this assumption is validated in Fig. 3.8 by the close fit between the measured reflectance waveform and the calculated fit (blue and red lines). From the fit, the final NL roughness is 8.86 ± 0.04 nm at 550 nm and 4.2 ± 0.1 nm from the 900 nm. The roughness from the 550 nm measurement agrees closely with the RMS roughness measured from atomic force microscopy of 9.7 ± 0.3 nm. However, the RMS roughness measured at 900 nm is significantly less. One possible reason for this difference is that the light at 900 nm is less sensitive to the nm scale roughness compared to light at 550 nm. This can be readily observed in the power spectral density (PSD) of the AFM images at the two wavelengths. At 550 nm the PSD is ≈ 3 times larger than at 900 nm, which would give a difference in the RMS roughness of a factor of 1.7 between 500 nm and 900 nm, close to the factor of 2 reported above. Another possible reason as to why the 900 nm RMS roughness is lower is the macroscopic roughness assumed in Eq. 3.4 is inadequate to describe the microscopic roughness of the NL and instead an effective-medium method should be used to describe the roughness.

3.2.2 NL Decomposition Kinetics and Kinetic Advancement

The NL decomposes at progressively faster rates as the *T* is increased. To account for the increase in the decomposition kinetics a method to compare the decomposition rates as *T* is varied is desired in order to fit the reflectance waveforms. From previous works, we know that the decomposition follows Arrhenius kinetics, with an activation energy, E_A, of 2.7±0.2 eV and a varying pre-exponential, A_0. From the previous work, A_0 does not depend on *T*, but only on the NH_3 gas flow and pressure [2].

For a NL that is heated and undergoes decomposition, the rate of change in the NL height, $h(t)$, (or volume) of the NL is

$$\partial h(t)/\partial t = -A_0 \exp[-E_A/k_B T(t)] \equiv -A_0 f(t), \quad (3.5)$$

where, k_B is the Boltzman constant. For simplification, a new function, $f(t) \equiv \exp[-E_A/k_B T(t)]$ has been defined, which allows the rescaling of time, *t*, to account for decomposition rate changes due to $T(t)$. Two regimes were used in our experiments, one where *T* is held constant and the other when *T* is a function of *t*. At constant $T = T_C$, $f(t)$ is constant, and Eq. 3.5 can be integrated to yield, $h(t) = h(t_0) - A_0 f(T_C)(t- t_0)$, where $h(t_0)$ is the initial NL thickness. For the other case where *T* depends on *t*, $h(t) = -A_0 \int_0^t f(t')\, dt' \equiv -A_0 F(t)$ and Eq. 3.4 must be integrated using a specified $T(t)$ schedule and subtracted from $h(t_0)$. We denote $F(t)$ as the "kinetic advancement", since it allows kinetic rates at different *T* to be compared directly. Since $f(t)$ is unitless, $F(t)$ has the unit of time. The units of A_0 are s^{-1} when the reflectance signal is plotted vs. $F(t)$ or nm/s when the transformed NL thickness is plotted vs. $F(t)$.

Note that a plot of $h(t)$ vs. $F(t)$ will yield a straight line with a slope of $-A_0$, because $h(t) = -A_0 F(t)$. The decrease in the NL thickness, $h(t)$, is modeled based on decomposition kinetics and shown in the top right corner of Fig. 3.9. The decrease in $h(t)$ was modeled using E_A = 2.7 eV, A_0 = 2.0×10^{10} nm/s, and a *T* ramp rate of 1 ºC/s from 550 to 1050 °C after which T_C = 1050 °C. In the main portion of Fig. 3.9, the kinetic advancement, $F(t)$, is next calculated using trial values for E_A of 1.0, 2.0, 2.7, and 4.0 eV and the same *T* ramp rate used to simulate the decrease in NL thickness is used to calculate $F(t)$. For each E_A, $F(t)$ is scaled by a constant (listed in the Fig. 3.9 caption) so that decrease in $h(t)$ as a function of $F(t)$ can be directly compared. As shown in Fig. 3.9, $h(t)$ vs. $F(t)$ is only linear for an E_A of 2.7 eV, which was used for the initial calculation of $h(t)$. For values of E_A different than 2.7 eV, the plot of $h(t)$ vs. $F(t)$ has noticeable curvature. While assuming that E_A is constant is a requirement for calculating the kinetic advancement, a varying E_A could also be used as long as the dependence of E_A on *T* is known explicitly.

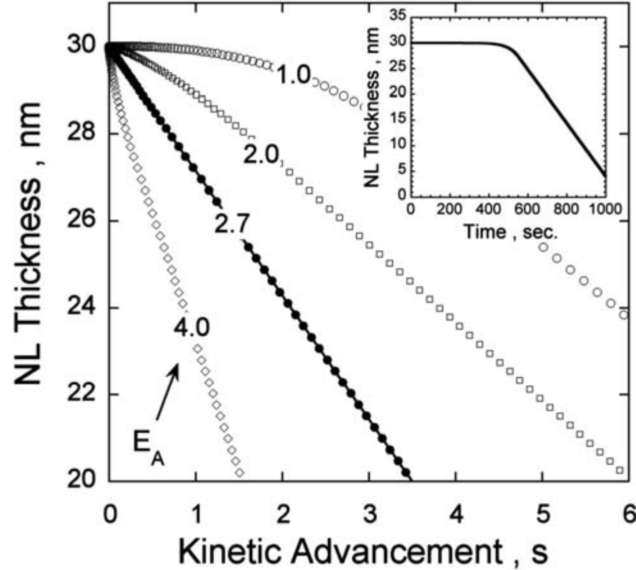

Fig. 3.9. The nucleation layer (NL) thickness is plotted vs. the kinetic advancement, *F*(*t*), for different activation energies, E_A. For the calculation, a NL decomposition rate based on an E_A of 2.7 eV, and a pre-exponential factor, A_0, of 1×10^9 nm/sec, is calculated over the *T* range of 500 to 1050 ºC at a rate of 1 ºC/sec. The calculated NL decomposition rate was integrated and subtracted from an initial NL thickness of 30 nm. Separately, *F*(*t*) was calculated using E_A values of 1.0, 2.0, 2.7, and 4.0 eV. In order to plot each of the NL thickness decreases vs. *F*(*t*), the x-axis was multiplied by 2×10^2 for 1 eV, 1.2×10^6 for 2.0 eV, 3.5×10^8 for 2.7 eV, and 1.5×10^{13} for 4.0 eV. Note that only the E_A of 2.7 eV gives a straight line, because this E_A was used in the initial calculation of the NL decomposition as discussed above.

The reflectance waveforms for four annealed NLs are shown in Fig. 3.10(a). For each of the NLs a different *T* ramp rate was used ranging from 20 to 50 ºC/min. As discussed in Section 3.1, the fit to the reflectance waveform (solid line) includes both the *T* dependent increase in *R* and the NL decomposition kinetics [8]. The decomposition fit was obtained by first assuming a value of A_0, second calculating *F*(*t*) using an E_A of 2.7 eV, and finally subtracting it from the initial NL thickness. A_0 was varied until a good match to the reflectance waveform was attained. For the waveforms shown in Fig. 3.10(a) an $A_0 = 2.1\times10^7$ s^{-1} provided a good fit for ramp rates of 20, 30, and 40 °C/min., while an $A_0 = 2.3\times10^7$ s^{-1} provided the best fit for the ramp rate of 50 °C/min.

To show the generalness of the technique, three additional reflectance waveform fits are shown in Fig. 3.11(a). These NLs were annealed using combinations of *P* and NH_3 flow rates that produced similar decomposition rates [8]. Since similar decomposition rates were targeted, the values of A_0 should be similar. At 500 and 150 torr, the A_0's are identical ($A_0 = 5.2\times10^7$ s^{-1}) as excepted and slightly lower ($A_0 = 4.5\times10^7$ s^{-1}) at 50 torr.

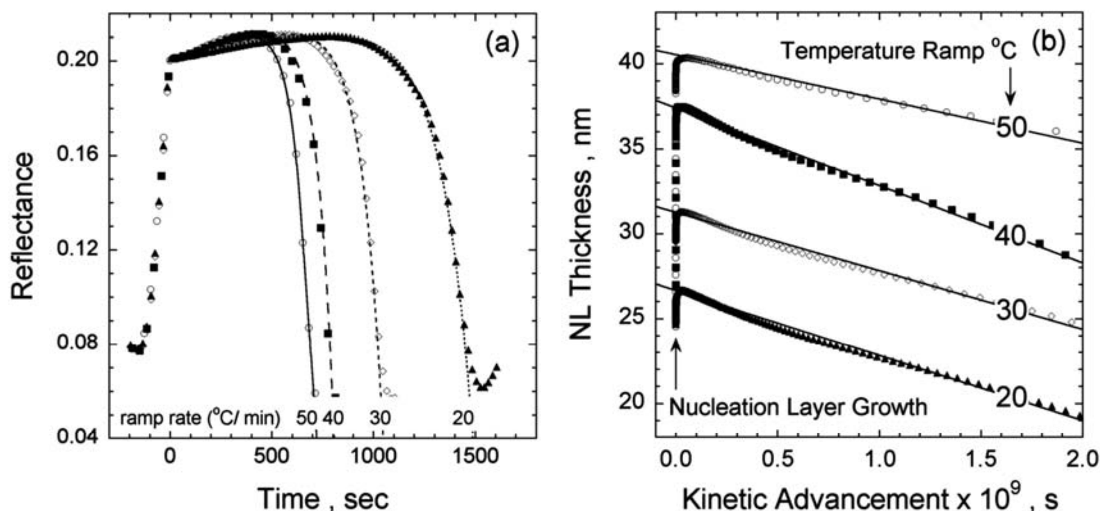

Fig. 3.10 (a) Reflectance waveforms are plotted for *T* ramp rates of 50 (open circles), 40 (closed squares), 30 (open diamonds), and 20 (closed triangles) ºC/min. Fits for each waveform as also plotted by solid lines following Eq. 3.4 and the decomposition kinetics. (b) The same reflectance waveforms in (a) are transformed to NL thickness and plotted as a function of the kinetic advancement factor, *F*(*t*). The waveforms measured with ramp rates of 50, 40, and 20 ºC are shifted along the y-axis.

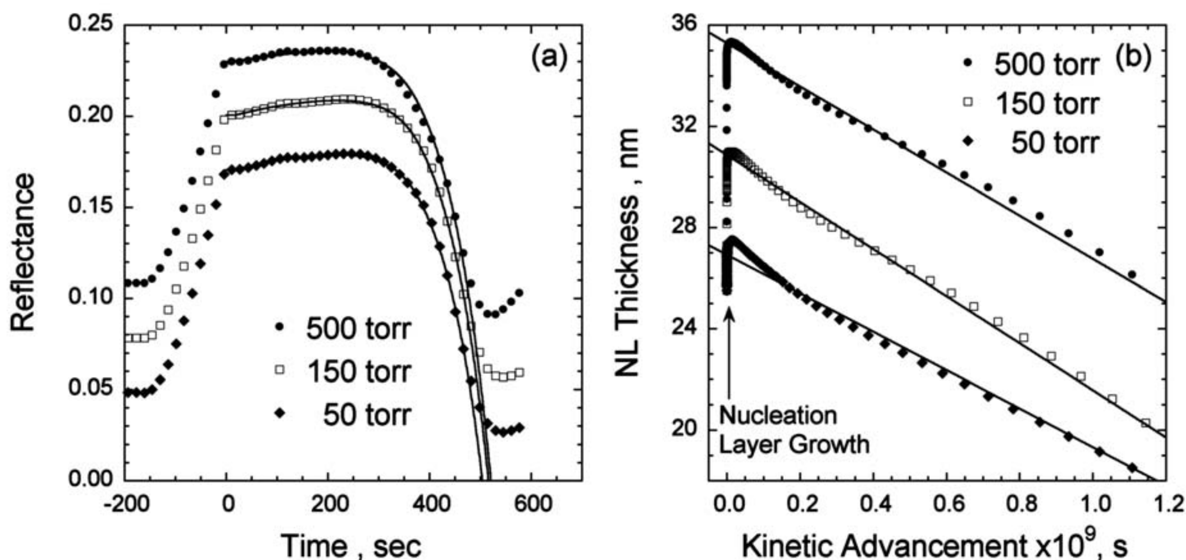

Fig. 3.11. Same as Fig. 10, except that the pressure and NH_3 flow conditions were chosen to produce similar NL decomposition rates.

The transformed NL thickness for Figs. 3.10(a) and 3.11(a) are plotted vs. $F(t)$ in Figs. 3.10(b) and 3.11(b). In Fig. 10(b) a linear fit is shown by a solid line with A_0 calculated from the slope for each T ramp rate. The values for A_0 are 2.6x10^9, 4.6x10^9, 3.4x10^9, and 3.8x10^9 nm/s for T ramps of 50, 40, 30, and 20 ºC, respectively. Independently, values of A_0 for R plotted vs. $F(t)$ and averaging the values for A_0 results in A_0=2.3x10^7 s^{-1} and A_0=3.7x10^9 nm/s, which are close to the A_0 values listed above for the direct fitting technique used in Fig. 3.10(a). Since a reflectance

value of 0.20 corresponds to a NL thickness of 30 nm, a factor of ≈ 150 is expected when comparing A_0 obtained from fitting the reflectance signal (as shown in Fig. 3.10(a)) compared to the NL thickness (as shown in Fig. 3.10(b)). Comparing the average A_0's listed above resulted in a factor of $(3.7x10^9/2.3x10^7) = 161$ which is close to the expected factor of 150. Fits similar to those shown in Fig. 3.10(b) are also derived and plotted in Fig. 3.11(b).

When plotting R (or NL thickness) as a function of $F(t)$ to extract A_0, the NL roughens for T above 960 ºC and this roughness will also decreases R, but at a much faster rate. The NL roughening will cause an observable decrease in the kinetic advancement plots. Therefore, only the reflectance signal before the NL roughening should be used to calculate A_0, which is the first 1/4 to 1/3 of the total decrease in the initial R.

3.3 Modeling optical reflectance for GaN growth on sapphire

In the past year, we have also developed a model to simulate reflectance waveforms for GaN growth on sapphire. The model is based on detailed studies of nucleation layer evolution as detailed in Ref. [13], analytical models to describe 3D island growth and coalescence and modifications to the virtual interface model [8]. These details were obtained from detailed reflectance measurements and atomic force microscopy images of paused growths. The model includes 1) temperature dependence of the optical constants for GaN and sapphire, 2) low temperature nucleation layer growth and annealing [13], 3) nucleation layer (NL) decomposition kinetics [2] and roughening, 4) high temperature 3D island growth followed by coalescence of the islands to form a smooth [1], and 5) wavelength of light used for the reflectance.

The morphological evolution of high temperature GaN growth on an annealed GaN nucleation layer (NL) is shown in Fig. 3.12. As shown in Fig. 3.12, the annealed GaN NL generates nuclei on which the high T GaN grows. As soon as the high T growth initiates, the GaN grain density is established, after which the GaN grains increase both vertically and laterally and eventually form a complete 2D coalesced film. (In Fig. 3.12 this time would be > 30 minutes.) For the progression of images shown in Fig. 3.12, the reflectance decreases from 0 min. to 3 min., then is near zero from 3 min. to 15 min., and then begins to increase after 15 min. during which time the GaN films begins to coalesce. For the image measured at 30 min. the optical reflectance is 0.09, which is approximately ½ of the final reflectance of 0.20. Note that near 9 min. of growth the film is not composed of discrete GaN grains but forms a percolated network of continuous interconnected regions. These connected regions are faceted similar to the SEM images of the GaN grains shown in Figs. 3.5(a) and 3.5(b).

To explain the growth evolution a 2 dimensional analytical growth model has been developed, which captures the granularity of the initial growth stages of GaN and the subsequent coalescence of the grains. Details of this model are shown in Fig. 3.13, where two different growth modes are represented. As shown in Fig. 3.13, the GaN grains are represented by trapezoids having a height, h, and a base width defined in terms of h, as αh. Using the definitions shown in Fig. 3.13, two different growth modes can be simulated depending on β which determines the length of the (0001) facet. For large β (as shown on the top of Fig. 3.13) the (0001) growth plane is large and 2D growth is modeled, while for the limit that $\beta \rightarrow 0$ the (0001) growth plane vanishes and 3D growth is modeled.

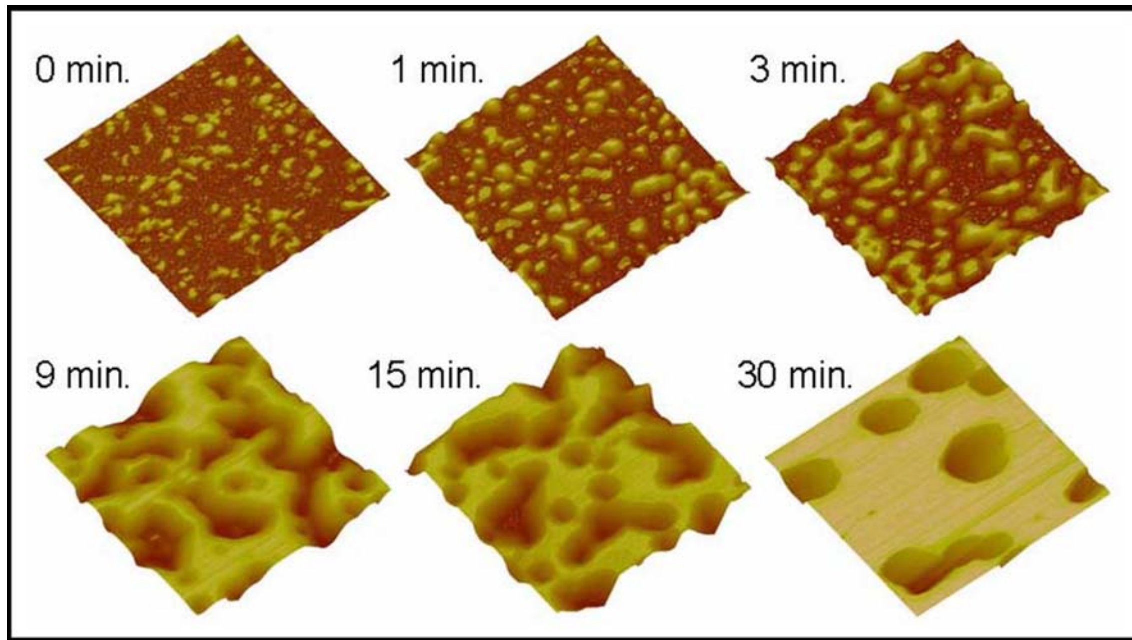

Fig 3.12. AFM images showing the morphological evolution of GaN grown on annealed GaN NLs. The images were obtained using the same growth sequence with the growth being stopped and quenched in N_2 and NH_3 to prevent further morphological changes. The images are 5x5 μm in size and 500 nm in height.

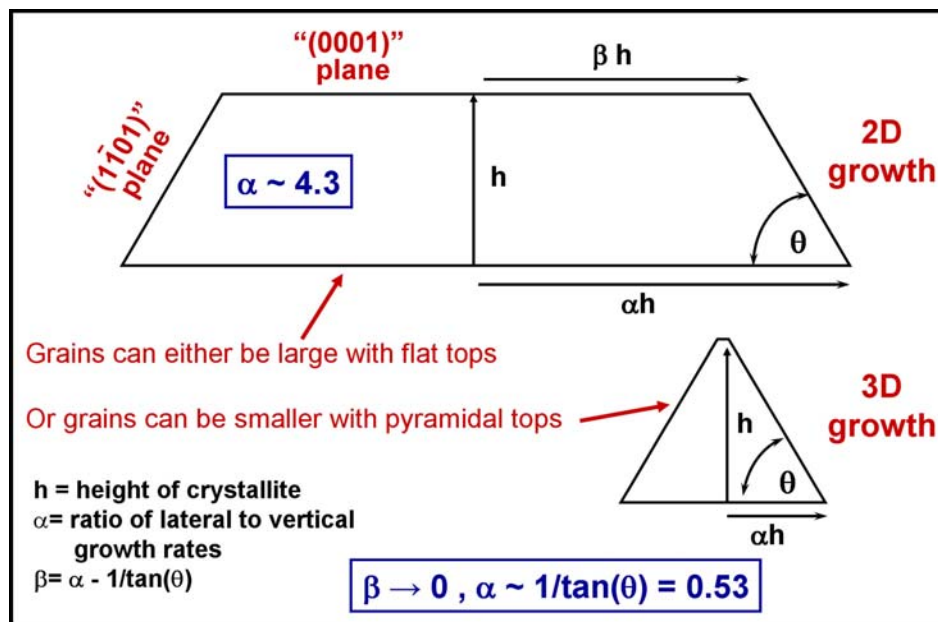

Fig. 3.13. Two different GaN grain geometries used in the growth modeling are shown. The top grain has a large (0001) facet (large *βh*) and effectively models 2D growth, while the bottom grain has a small (0001) facet (*β* → 0) and effectively models 3D growth. The definitions for the grain parameters are shown in the image. θ is the angle between the (0001) and (1$\bar{1}$01) facets, which is approximately 62°.

For the model the parameters, β (where $\beta = \alpha - 1/\tan(\theta)$), h, growth rate, G, and the distance between nuclei, d, are set. If the grains have a lateral to vertical growth rate ratio defined by α, and a coverage of initial GaN grains is defined by ζ, the roughness of the growing films is described by,

$$\sigma = h[\exp(-2\beta h) - \exp(-4\beta h)]^{1/2} . \quad (3.6)$$

After these parameters are set the reflectance waveform can be simulated using Eq. 3.3 and Eq. 3.6 to simulate the growth images shown in Fig. 3.12. An additional advantage of this model is that the fraction of defects that reach the surface is give by $\zeta(\alpha - 1/\tan\theta)/\alpha$.

The roughness and expected reflectance attenuation is shown in Fig. 3.14. For this simulation the spacing between grains was 200 nm, G was 600 nm/hour, and h is the film thickness/d. As shown in Fig. 3.14(a) the roughness is calculated using Eq. 3.6 for different values of α ranging from 1 to 4. Note that for this choice of parameters the roughness approaches 150 nm for $\alpha = 1$ which is close to the 3D growth mode. For $\alpha = 4$ the film only roughens to only 20 nm. Using the values for roughness calculated from Eq. 3.6 the reflectance attenuation can be calculated as shown in Fig. 3.14(b). For $\alpha = 4$ there is no noticeable attenuation of the reflectance signal, while for $\alpha = 1$, the attenuation is significant and qualitatively matches the reflectance waveform shown in Fig. 3.3(a).

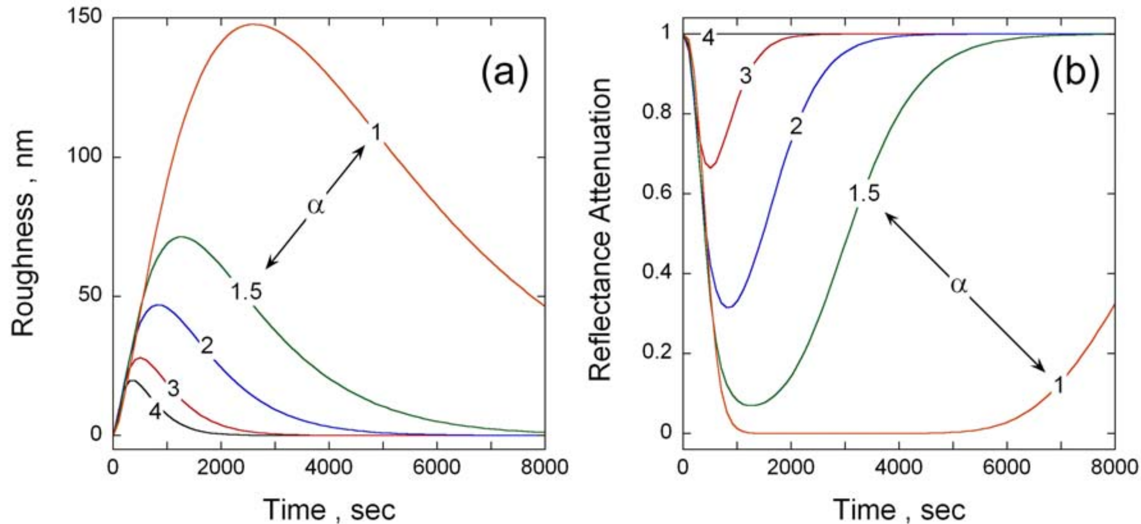

Fig. 3.14. Calculated roughness (a) and reflectance attenuation (b) based on the growth model described by Eq. 3.6. For this calculation a distance between nuclei of 200 nm and a growth rate of 600 nm/hour were assumed.

We next assembled the physical changes that occur from NL growth, NL annealing, and initial grain growth and simulate the full reflectance waveform for GaN growth. We show the details in the reflectance waveform fit for an annealed NL in Fig. 3.15. In Fig. 3.15(a), the increase in the reflectance signal due to the increase in the sapphire and GaN optical constants is shown. Previously, we have measured that the optical constant increases linearly as the temperature is increased [8]. In Fig. 3.15(b) the NL decomposition is modeled following the kinetics described in Ref. [2]. The blue line represents the integrated form of the Arrhenius

formula for the NL decomposition and the green line represents the GaN nuclei decomposition as shown in Ref. [1].

The difference in the decomposition rates of the NL compared to the nuclei is approximately 6. By combining the two decomposition rates the difference between the decomposition and the reflectance waveform is due to roughening of the NL as previously described [1]. Dividing reflectance signal by the expected NL decomposition (blue and green lines) gives the attenuation of the reflectance signal. The roughness that corresponds to this reflectance attenuation is 33 nm which is close to the roughness measured by AFM of 32 nm [1]. These results in Fig. 3.15 demonstrate that the decrease in the reflectance signal as the NL is heated is due to two sources; the NL decomposition and the NL roughening.

Finally, in Fig. 3.16, we show GaN reflectance waveforms from Ref. [14] and simulated waveforms following Eqs. 3.3, 3.4, and 3.6. The first waveform from Ref. [14] shows the growth of a thick GaN NL (100 nm) followed by annealing to 1050 °C and subsequent growth. In Ref. [14] the roughness and its influence on the reflectance signal is modeled after a simple exponential which decreases for increasing time. Using the formula a simulated waveform is shown in Fig. 3.16(b), which mimics all major features of the experimental waveform shown in Fig. 3.16(a).

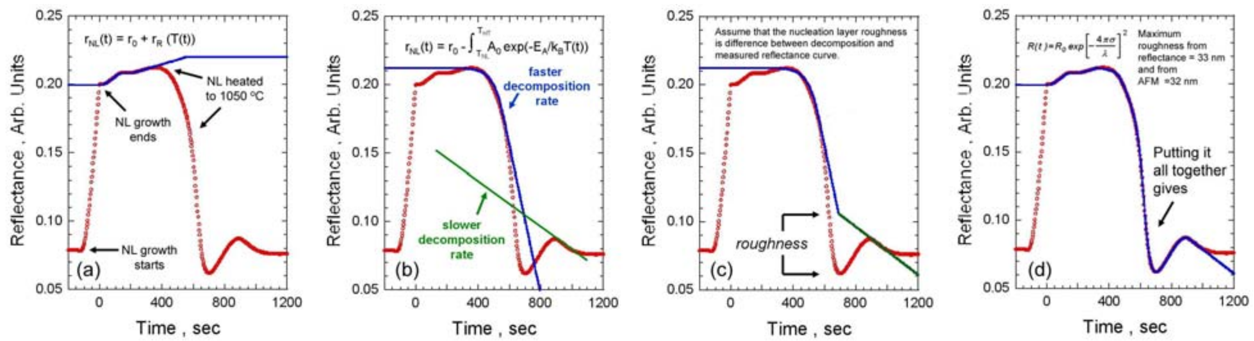

Fig 15. Experimental GaN NL waveform evolution as it is heated from 550 to 1050 ºC. First the NL is grown until a reflectance value of 0.20 is attained. After holding for 15 seconds the NL is heated using two different T ramps. In (a), the blue curve is a fit based on the increase in the optical constants for GaN and sapphire. The decrease in the reflectance waveform beginning near 800 ºC is due to NL decomposition and the blue and green curves in (b) are fits to the decomposition kinetics for the as grown NL (blue) and the GaN nuclei (green) that form on the NL during annealing. In (c), the combined decreases due to decomposition are combined and the difference between these curves (blue and green) and the reflectance signal is due to roughening of the NL. Dividing the curves in (c) by the reflectance signal gives the blue curve in (d). From the difference between the curves in (c) and (d) a RMS roughness of 33 nm is obtained which compares well to 32 nm roughness measured using AFM.

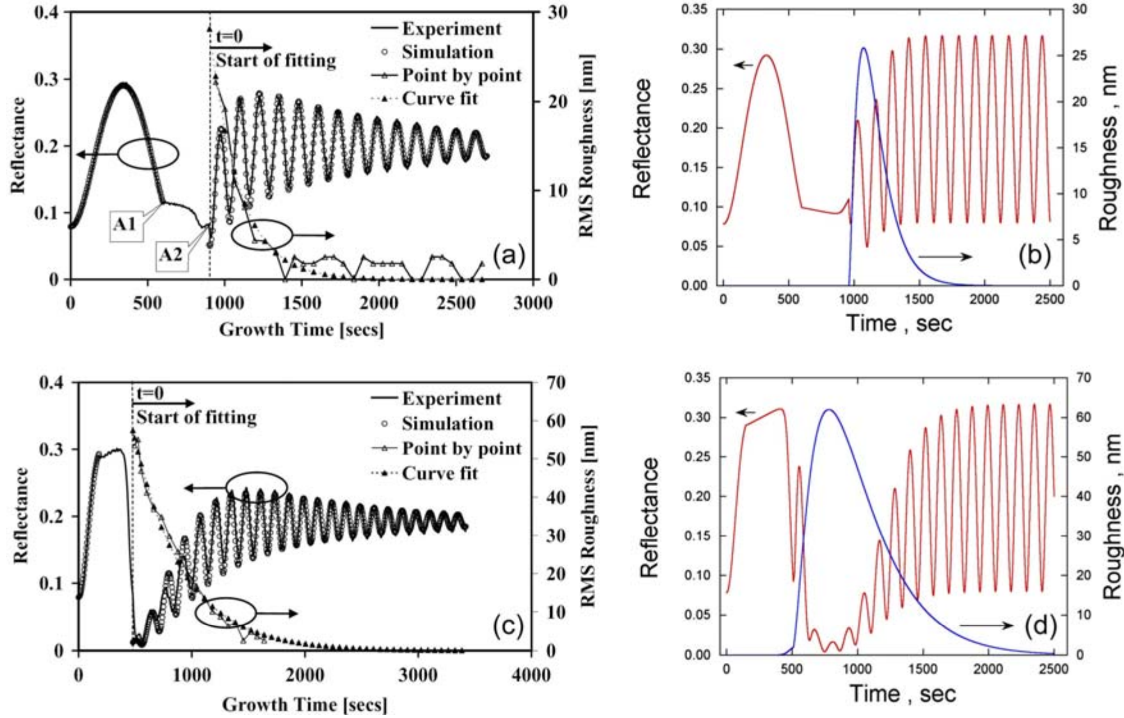

Fig. 16. Experimental reflectance waveform from Ref. [14] are shown in (a) and (c) and the corresponding model fits in (b) and (d). The damping of the oscillations in (a) and (c) are due to growth non-uniformity across the wafer which has not been built into the model. The initial growth roughness is shown in (a) and (c) by the open triangles and in (b) and (d) by the blue curve.

Note especially that the initial roughness at the start of high *T* growth is roughly 25 nm in both Figs. 3.16(a) and 3.16(b). The damping of the growth oscillation in Fig. 3.16(a) is due to growth non-uniformity across the wafer, which was not put into the calculation show in Fig. 3.16(b). A second waveform from Ref. [14] is shown in Fig. 3.16(c) along with the accompanying simulated waveform in Fig. 3.16(d). Here a thinner GaN NL was used (45 nm) and there is an increase in the roughness of approximately 60 nm observed in the fit in Fig. 3.16(c) and in the simulated waveform shown in Fig. 3.16(d). The major difference between the experimental (Fig. 3.16(c)) and simulated waveform (Fig. 3.16(d)) is the initial increase in the reflectance waveform near 500 seconds in Fig. 3.16(d). This increase is due to improperly matching the roughness between the annealed NL and the initial GaN grain model described by Eq. 3.6. Improving this part of the simulation is work that is currently in progress.

3.4 References

[1] D. D. Koleske, A. J. Fischer, A. A. Allerman, C. C. Mitchell, K. C. Cross, S. R. Kurtz, J. J. Figiel, K. W. Fullmer, and W. G. Breiland, Appl. Phys. Lett. 81 (2002) 1940.

[2] D. D. Koleske, M. E. Coltrin, A. A. Allerman, K. C. Cross, C. C. Mitchell, and J. J. Figiel, Appl. Phys. Lett. 82 (2003) 1170.

[3] S. R. Lee, A. M. West, A. A. Allerman, K. E. Waldrip, D. M. Follstaedt, P. P. Provencio, D. D. Koleske, and C. R. Abernathy, Appl. Phys. Lett. Submitted (2005)
[4] D. M. Follstaedt, N. A. Missert, D. D. Koleske, C. C. Mitchell, and K. C. Cross, Appl. Phys. Lett. 83 (2003) 4797.
[5] D. M. Follstaedt, P. P. Provencio, N. A. Missert, C. C. Mitchell, D. D. Koleske, A. A. Allerman, and C. I. H. Ashby, Appl. Phys. Lett. 81 (2002) 2758.
[6] H. Fujikura, K. Iizuka, and S. Tanaka, Jpn. J. Appl. Phys. 42 Part 1 (2003) 2767.
[7] A. E. Wickenden, D. D. Koleske, R. L. Henry, R. J. Gorman, M. E. Twigg, M. Fatemi, J. J. A. Freitas, and W. J. Moore, J. Electron. Mat. 29 (2000) 21.
[8] D. D. Koleske, M. E. Coltrin, and M. J. Russell, J. Cryst. Growth in press (2005)
[9] W. G. Breiland and K. P. Killeen, J. Appl. Phys. 78 (1995) 6726.
[10] K. Hiramatsu, S. Itoh, H. Amano, I. Akasaki, N. Kuwano, T. Shiraishi, and K. Oki, J. Cryst. Growth 115 (1991) 628.
[11] J. C. Stover, Optical Scattering: Measurement and Analysis, SPIE-the International Society for Optical Engineering, Bellingham, WA, 1995.
[12] N. A. Sanford, L. H. Robins, A. V. Davydov, A. Shapiro, D. V. Tsvetkov, A. V. Dmitriev, S. Keller, U. K. Mishra, and S. P. DenBaars, J. Appl. Phys. 94 (2003) 2980.
[13] D. D. Koleske, M. E. Coltrin, K. C. Cross, C. C. Mitchell, and A. A. Allerman, J. Cryst. Growth 273 (2004) 86.
[14] R. S. Balmer, C. Pickering, A. J. Pidduck, and T. Martin, J. Cryst. Growth 245 (2002) 198.

Distribution

2	MS 0601	J.R. Creighton
2	MS 0601	D.D. Koleske
1	MS 0601	R.M. Biefeld
1	MS 0601	G.T. Wang
1	MS 0601	A.A. Allerman
1	MS 0601	S.R. Lee
1	MS 0601	M.E. Coltrin
1	MS 1206	C.C. Mitchell
1	MS 0670	W.G. Breiland
1	MS 9018	Central Technical Files, 8945-1
2	MS 0899	Technical Library, 9616
1	MS 0123	LDRD Donna Chavez, 1011